

## RESEARCH ARTICLE

WILEY

# The mid-latitude hydrolaccolith of the Spanish Central System (Southern Europe): A top-to-bottom integration of geomatic, geophysical and sedimentary datasets for characterising a singular periglacial landform

Javier Fernández-Lozano<sup>1</sup>  | Valentí Turu<sup>2</sup> | Rosa M. Carrasco<sup>3</sup>  |  
Rodrigo L. Soteres<sup>4,5</sup> | Jesús Sánchez-Vizcaino<sup>3</sup> | Theodoros Karampaglidis<sup>3</sup> |  
Xavier Ros<sup>2</sup> | Oscar Merlo<sup>6</sup> | Javier Pedraza<sup>7</sup>

<sup>1</sup>Departamento de Tecnología Minera, Topografía y Estructuras, Universidad de León, León, Spain

<sup>2</sup>Fundació Marcel Chevallier, Edifici Socio-Cultural de La Llacuna, Andorra la Vella, Andorra

<sup>3</sup>Departamento de Ingeniería Geológica y Minera, Universidad de Castilla-La Mancha, Toledo, Spain

<sup>4</sup>Centro de Investigación GAIA-Antártica, Universidad de Magallanes, Punta Arenas, Chile

<sup>5</sup>Centro Internacional Cabo de Hornos (CHIC), Universidad de Magallanes, Puerto Williams, Chile

<sup>6</sup>Departamento de Ingeniería Civil y de la Edificación, UCLM, Ciudad Real, Spain

<sup>7</sup>Departamento de Geodinámica, Estratigrafía y Paleontología, Universidad Complutense de Madrid, Madrid, Spain

## Correspondence

Javier Fernández-Lozano, Departamento de Tecnología Minera, Topografía y Estructuras, Universidad de León, Campus de Vegazana s/n, León 24071, Spain.  
Email: [jferl@unileon.es](mailto:jferl@unileon.es)

## Funding information

Castilla La Mancha University Research Group, Grant/Award Number: 2023-GRIN-34112; Marcel Chevalier Earth Science Foundation; Spanish Ministry of Science and Innovation, Grant/Award Number: PID2020-117685GB-I00

## Abstract

Permafrost study in the Spanish Central System (~41°N) has remained elusive in past decades. Although numerous periglacial features have been described, none has yielded conclusive information about the existence/distribution of permafrost across these mountains. This work focuses on integrating light detection and ranging and unmanned aerial vehicle data with geophysical methods and sedimentary records, along with preliminary thermal information, for the comprehensive study of a frost mound. The singularity of this feature resides in its location, currently dominated by a seasonal frost regime, and its size reaching 59 m long, 22.5 m wide and 4 m high, representing the largest landform of this type in Iberia. From top-to-bottom, the internal structure comprises three resistivity units (G1, G2 and G3). The most superficial unit (G1) consists of a sequence of burial soils alternating with sand and silts, with pebbles and gravel at the bottom, followed by a high porous layer that belongs to a landslide deposit (G2), likely composed of gravel and pebbles laying over unit G3 (bedrock). Calibrated <sup>14</sup>C ages suggest this landform formed at least ~4300 years ago during the mid-Holocene. Finally, the preliminary surface thermal map indicates the presence of sectors affected by strong thermal gradients likely driven by water table variations. Our results conclude that the dynamics are primarily controlled by the seasonal frost regime influencing local subsurface drainage, which allows us to classify this landform as a hydrodynamic pingo-like structure. We also demonstrate that our approach is suitable for assessing the evolution of this type of periglacial landform. Implementing long-lasting annual monitoring programmes would help to understand local periglacial dynamics better.

## KEYWORDS

frost mound, geophysical and sedimentological record, LiDAR, Spanish Central System, UAVs

This is an open access article under the terms of the [Creative Commons Attribution](https://creativecommons.org/licenses/by/4.0/) License, which permits use, distribution and reproduction in any medium, provided the original work is properly cited.

© 2023 The Authors. *Land Degradation & Development* published by John Wiley & Sons Ltd.

## 1 | INTRODUCTION

The term *hydrolaccolith* is sometimes associated with those of *pingo*, *palsa*, *cryo-laccolith* and *blister frost* to name certain conical mounds caused by seasonal soil swelling in permafrost areas, but its use in this context is ruled out (Harris et al., 1988; Van Everdingen, 1998). However, it has also been used to refer to a convergent morphology with the previous ones but associated with the subsurface water flow variations and the seasonal ice-thaw cycles in permafrost-free regions (French, 1996; Ward, 2004; Worsley, 2004). This is the use of the term in the present work.

Most *hydrolaccolith*-like landforms have been identified in a wide variety of polar and subpolar regions and mountain permafrost terrain, particularly in the Northern Hemisphere (Frenzel, 1959; Mackay, 1998; Woolderink, 2014). However, little is known about the seasonal periglacial environments at temperate latitudes where such features are uncommon (Murton, 2021). Therefore, these features are of great interest to the scientific community because they could provide key insights to understand better processes and control factors involved in their formation, as well as the local environmental evolution (Ward, 2004; Woolderink, 2014; Worsley, 2004).

In Iberia, these periglacial landforms have been identified in most of the major mountain ranges. For instance, in the Pyrenees, frost mounds have been described and linked to the presence of permafrost (Serrano et al., 2019). In the Spanish Central System and the Leonese Mountains, however, similar features were also documented and classified as *hydrolaccoliths* associated with the seasonal frost regime (Centeno et al., 1983; Fernández-Lozano & Andrés-Bercianos, 2020; Molina & Pellitero, 1982; Pedraza, 1994). Recently, the presence of a well-developed *hydrolaccolith* has been reported in the Calderuelas Valley, within the Guadarrama National Park, located in the eastern sector of the Spanish Central System (Carrasco et al., 2020). Although the local ground thermal regime is unknown, nearby mountain massifs have been reported free of permafrost with annual soil temperatures over 0°C at 2000 m a.s.l. (Andrés-de Pablo & Palacios-Estremera, 2010; Palomo-Segovia, 2012). Therefore, due to their singularity in this Mediterranean mountain range, assessing their morphology and seasonal geometry variations along with sub-surface temperatures and inner structure may help to understand their representativity in terms of genesis and evolution. In addition to the key scientific value, understanding the activity of these periglacial landforms offers new insights to promote effective management plans in protected natural areas that aim at their conservation by administration stakeholders and public awareness.

The study of frost mounds has often been focused on spatial distribution and geometrical analysis (i.e., shape and size) throughout traditional low-resolution methods such as aerial orthoimages and visual field interpretation. However, the implementation of geomatic technologies such as airborne light detection and ranging (LiDAR) technology and unmanned aerial vehicles (UAVs) provides an effective method for detailed mapping by producing digital elevation models (DEMs) and orthomosaics of high-resolution (i.e., centimetric) that afford precise analysis of a wide range of glacial and periglacial

processes. Geomatic technologies have significantly contributed to filling the gap between traditional terrestrial, aerial and satellite data, providing vital information in inaccessible or remote areas (Abermann et al., 2010; Colucci et al., 2016; Fernández-Lozano & Andrés-Bercianos, 2020; Jones et al., 2013; Migoñ et al., 2013; Śledź et al., 2021). For instance, the study of periglacial talus slopes through the detection and spatial analysis of 3D models using sequential measurements provides insights into the dynamics of these landforms, such as volumetric changes and horizontal displacements, allowing inferences about the controlling factors that promote their genesis and evolution (Hendrickx et al., 2017, 2020). Luo et al. (2019) also carried out similar analyses using both technologies to monitor the evolution of frost heave and thaw of frost mounds and their impact on engineering infrastructure. These surface surveying techniques, however, require other subsurface methods to explore in detail the inner structure of these periglacial landforms. Amongst the most extensive subsurface methods, seismic and electrical resistivity has been widely used for understanding process–form relationships in glacial and periglacial environments (Carrasco et al., 2018; Doolittle & Nelson, 2009; Munroe et al., 2007; Schennen et al., 2016). These methods can be expanded empirically with the sedimentary record obtained from drill cores to validate further geophysical interpretations (Granja-Bruña et al., 2021; Leopold & Völkel, 2003; Voelkel et al., 2001).

The Calderuelas *hydrolaccolith* represents a singular feature of great relevance due to its genetic and climatic implications regarding the poorly constrained regional present-to-past periglacial conditions. The new surface and subsurface geological techniques provide valuable insights that reinforce prior analysis from Carrasco, Pedraza, et al. (2020) and shed light on the mechanisms that govern the genesis and evolution of the *hydrolaccolith*. This information will also contribute to rising measurements for the future preservation of this singular landform.

This study follows a multidisciplinary approach based on geophysical, geomatic, sedimentary and chronological data along with preliminary thermal regime analysis that provides “top-to-bottom” information to characterise the *hydrolaccolith* of the Calderuelas Valley at Sierra de Guadarrama National Park. This paper aims to establish the geological framework in which to perform future long-term analysis of the current evolution using permanent stations that will provide systematic measurements to assess the ongoing dynamics of the *hydrolaccolith* further.

## 2 | REGIONAL CONTEXT

The study area is in a high mountainous region of the eastern sector of the Spanish Central System (Sierra de Guadarrama National Park), locally known as Alto de las Calderuelas (Figure 1). Its mean elevation reaches over 1800 m a.s.l., whilst the maximum height is reached towards the southwest at 2077 m a.s.l. in La Flecha peak. From a physiographic point of view, this massif exhibits a NE–SW orientation, standing out over the Duero and Tagus Mesetas at the north and south, respectively. The local topography comprises subdued peaks

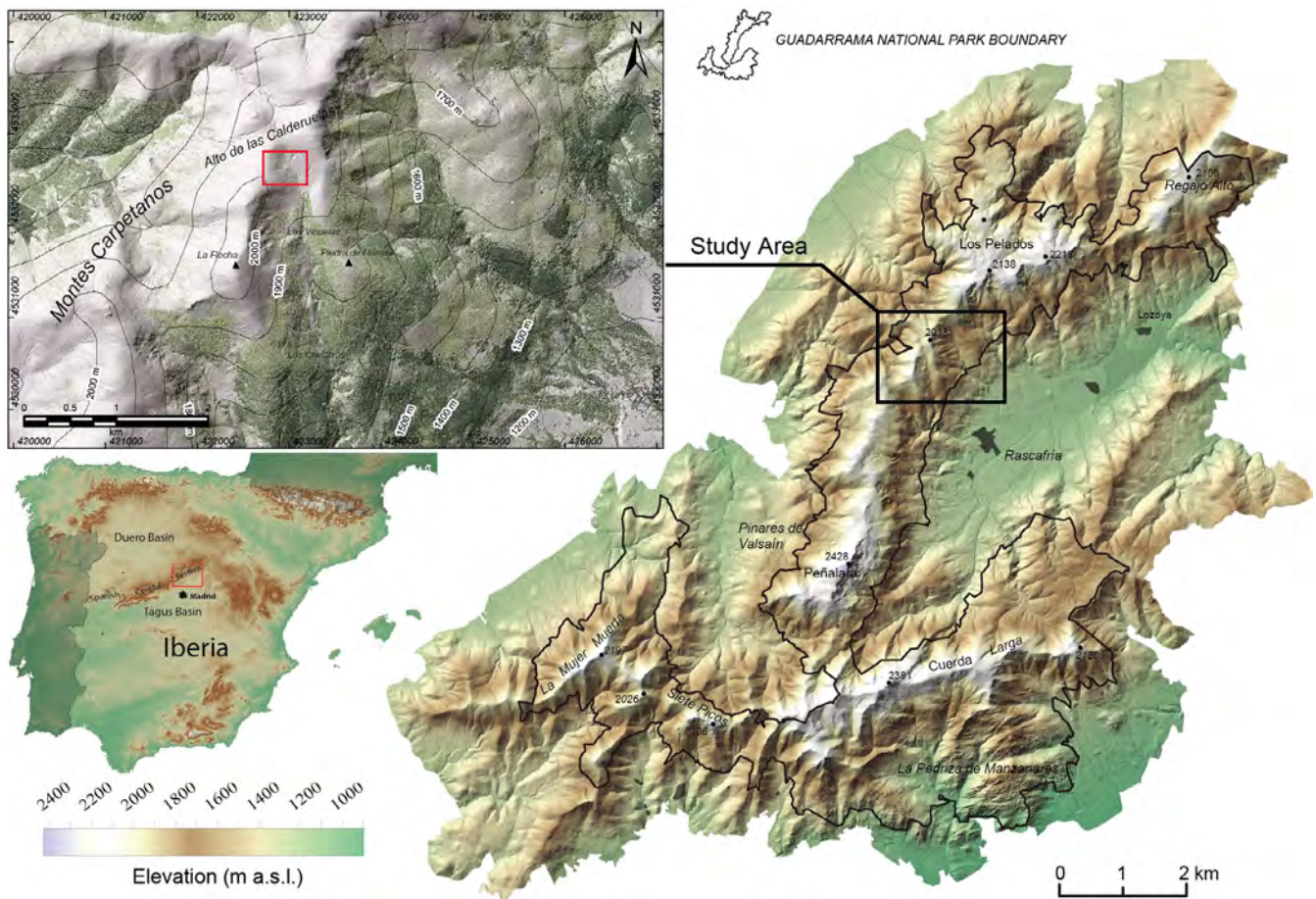


**FIGURE 1** Sketch map of the study area in the Guadarrama National Park (Spanish Central System). [Colour figure can be viewed at [wileyonlinelibrary.com](https://onlinelibrary.wiley.com/doi/10.1002/ldr.4968)]

with slopes between  $60^\circ$  and  $85^\circ$  in the headwalls. The northern and southern flanks of these mountains show a strong asymmetric morpho-structure with rugged southern hillslopes and smoother gradients to the north.

Meteorological data for the 2013–2023 period show mean annual temperature oscillation between  $-10$  and  $26.3^\circ\text{C}$  over 1600 m a.s.l. Annual precipitation varies from 1200 to 2500 mm, including snow between November and May (open data AEMET, 2023, <https://opendata.aemet.es/>). Soil temperature measurements at 10 cm depth between 2001 and 2011 in nearby sectors range between  $-4.4^\circ\text{C}$  (December) and  $27.5^\circ\text{C}$  (July) (i.e., Peñalara Massif,  $\sim 2000$  m a.s.l.; Palomo-Segovia, 2012). The general regime of mean soil temperatures presents cold conditions between September and May and warmer temperatures from June to August. In addition, according to the Köppen-Geiger classification, the area presents a Mediterranean mountain climate with strong continental influence (Dsb and DsC).

The regional geology forms part of the Central Iberian Zone (easter Iberian Massif), which in this area mainly consists of high-grade pre-Ordovician crystalline basement rocks, principally glandular orthogneiss with intercalated leucogneiss. Metasedimentary rocks in the area are scarce and comprise semipellitic paragneiss and alternating quartzites (Arenas-Martínez et al., 1991). These rocks were

strongly deformed during the Variscan orogeny (Macaya et al., 1991). The N–S orientation of the valleys is controlled by the presence of reactivated Alpine faults responsible for the asymmetric morphology of the chain and the presence of steeped blocks that influence the position of valleys and mountains and are controlled by the most recent Alpine tectonics (De Vicente et al., 2007, 2018).

The Calderuelas hydrocololith (Figure 2a) is situated close to the headwall of a glacial cirque in a U-shaped valley that was most likely occupied by a small mountain glacier between  $\sim 26$  ka ( $k_a = 1000$  - years ago) and  $\sim 11$ – $12$  ka spanning from the last glacial maximum to the early Holocene (Carrasco et al., 2016, 2022; Palacios et al., 2012). Local surficial processes are associated with frost and thaw cycles commonly over 1500 m a.s.l. (Palomo-Segovia, 2012). Ground swelling extends across the right bank of the Calderuelas Creek headwaters near the mountain summit, although the development of other minor structures, such as water blisters, is a common feature at the bottom valley (Figure 2b). The presence of solifluction lobes is associated with periglacial dynamics and highlights the location of active slopes in the valley. These deposits partially cover the basal substrate in the lower part of the hillsides. Solifluction lobes often comprise thin superficial formations ( $\sim 2$ – $6$  m), mainly corresponding to colluvium and debris slope deposits (Ruiz-García et al., 1991) with small pools

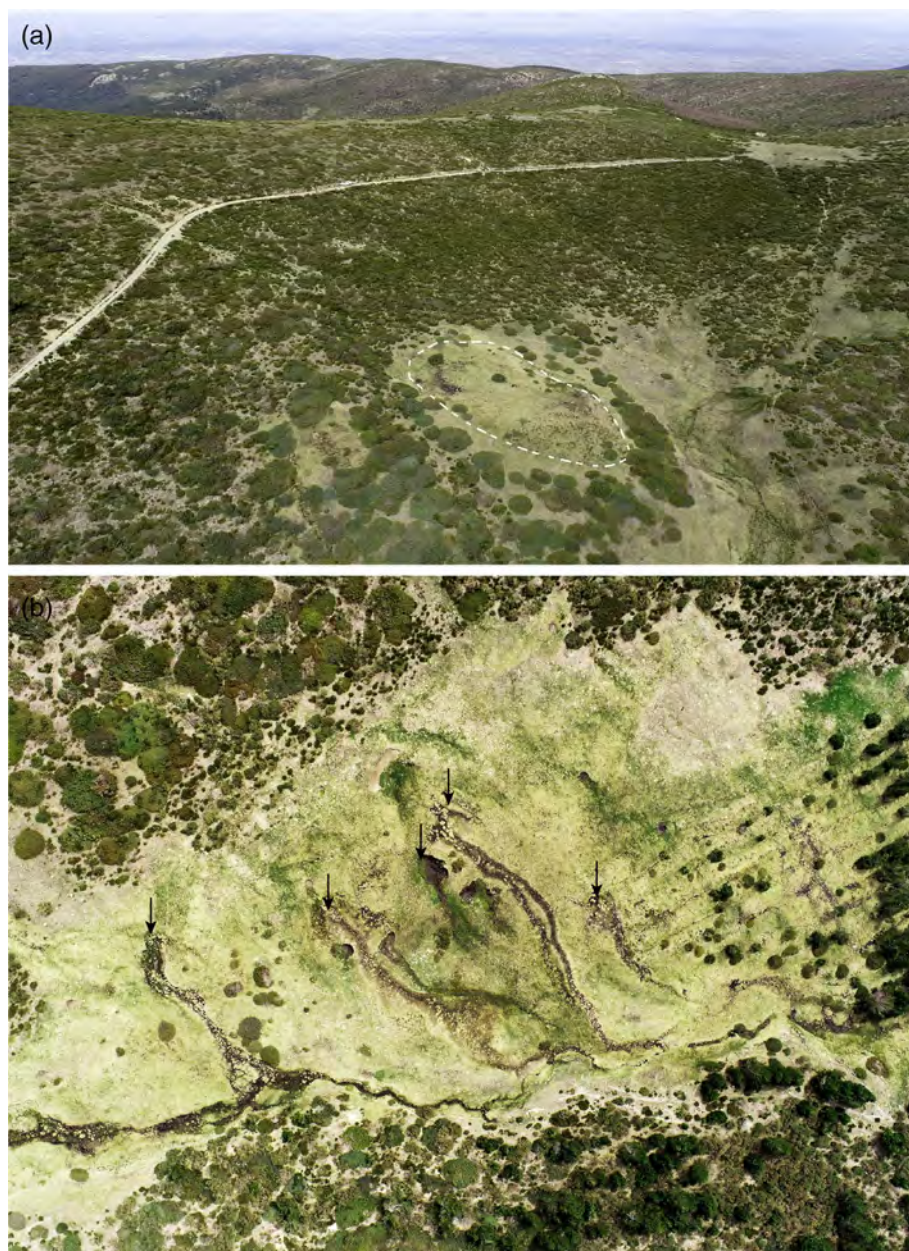


**FIGURE 2** (a) Panoramic view of the Calderuelas hydrolaccolith. (b) Water blisters (black arrows), also called in the Central System “bojas.” [Colour figure can be viewed at [wileyonlinelibrary.com](https://onlinelibrary.wiley.com/doi/10.1002/ldr.4968)] [Colour figure can be viewed at [wileyonlinelibrary.com](https://onlinelibrary.wiley.com/doi/10.1002/ldr.4968)]

and ponds. Similar slope configurations have been extensively studied previously in the region (López-Sáez et al., 2020; Turu et al., 2018, 2021).

### 3 | METHODOLOGY

In this work, we have adopted a multidisciplinary approach to afford a “top-to-bottom” characterisation of the Calderuelas hydrolaccolith. Firstly, historic identification was carried out using aerial orthoimages and topographic maps from different dates. Secondly, geomatic tools allowed us to obtain the morphological expression and dimensions of the landform. Finally, geophysics and auger coring provided essential information concerning the subsurface structure of the landform. Each methodological approach is described in detail below.

#### 3.1 | Surface characterisation

##### 3.1.1 | UAV high-resolution mapping

Surface morphological characterisation was performed by comparing aerial orthoimages from 1946 to 2017 from American Flight and Plan Nacional de Ortofotografía Aérea (PNOA: 2004, 2006, 2008, 2009, 2010, 2011, 2014 and 2017) with image resolution between 0.5 and 0.25 m. Although the best resolution to constrain the dimensions of the structure was achieved with the 2017 series. The cartographic repository was downloaded from the Spanish Organismo Autónomo Centro Nacional de Información Geográfica (OACNIG at <https://centrodedescargas.cnig.es/CentroDescargas/index.jsp>).

In addition, LiDAR data from the PNOA database with a point cloud density of 0.5 p/m<sup>2</sup> from the Spanish 1st flight coverage (2010)

to obtain 1 m resolution Digital Terrain Model (DTM) (Z-RMSE  $\sim 0.2$  m). The DTM was used for the morphological analysis using relief visualisation techniques (terrain slope, openness-negative, principal component analysis and sky view factor) based on visual enhancement tools developed by Kokalj et al. (2011) and Štular et al. (2012) and following the methodological approach for geomorphological analysis by Carrasco et al. (2020) and Fernández-Lozano et al. (2019).

The surface analysis was completed by monitoring the seasonal topographic variations observed from UAV-derived photogrammetric products: orthomosaics and digital surface models (DSMs). Two flights (in February and July 2022) were performed using a DJI Phantom 4-RTK UAV and the D-RTK 2 mobile station (accuracy  $< 0.02$  m; Figure 3a). RTK file was post-processed using RINEX files from Instituto Geográfico Nacional GNSS Permanent Stations (PNAV-Puerto Navacerrada).

The terrain awareness option was used during the flight to maintain a 50 m flying height for the whole working area regardless of the relief variations. A grid flight plan allowed the capture of aerial images covering a total area of 11.8 ha. The final ground sampling distance (GSD) was  $< 0.002$  m/pixel, and the RMS Error was X, Y and Z  $< 0.01$  m. Processing of the images based on bundle adjustment and

point cloud densification was performed using Pix4D<sup>®</sup> software and computing projects with 125 (February) and 390 images (July). Topographic changes were measured by DSM subtraction from both UAV flights using Global Mapper<sup>®</sup> and Oasis Montaj<sup>®</sup> software.

### 3.1.2 | Surficial temperature measurements

To provide first-order interpretations of the mechanisms that may govern the cryogenic evolution of the frost mound, a thermal gradient map was also carried out by systematic measuring between the winter (February) and the summer (July) across a  $5 \times 5$  m grid covering the whole structure. The rationale behind this was to interpret the observed variations on the surface and subsurface thermal gradient responsible for the evolution of the frost mound. During the winter, frost and thaw cycles can be easily analysed and interpreted, whilst, during the summer, the presence of groundwater can be detected through thermal data. Altogether, these data can provide information of great significance to analyse the process behind the evolution of the frost mound. Surface thermal measurements were obtained using a Flir E8-XT<sup>®</sup> thermal camera ( $320 \times 240$  pixels and spectral range 7.5–13  $\mu\text{m}$ ) with a temperature range between  $-20^\circ\text{C}$



**FIGURE 3** (a) UAV flight using a D-RTK GNSS station and a DJI Phantom 4-RTK system. (b) Thermal surveying using a FLIR camera. (c) Geoelectric tomography surveying and (d) drill-core tasks. [Colour figure can be viewed at [wileyonlinelibrary.com](https://onlinelibrary.wiley.com/doi/10.1002/ldr.4968)]

and 550°C and thermal sensitivity of  $\pm 0.05^\circ\text{C}$  (Figure 3b). Whereas subsurface temperature (10 cm depth) was acquired using a Delta OHM HD2307.0 RTD<sup>®</sup> Thermometer ( $-200^\circ/650^\circ\text{C}$ ) with  $\pm 0.05^\circ\text{C}$  accuracy. Finally, a 2D Fourier transform was carried out over the thermal gradient map to characterise the wavelength of the thermal anomaly observed for the summer temperature map. Filtering of thermal data was done by applying a Butterworth Filter in Oasis Montaj<sup>®</sup>, which provides low and high pass filtering, allowing control of the sharpness of the filter around the wavelength cut-off.

## 3.2 | Subsurface characterisation

### 3.2.1 | Geoelectric surveying

Two different geophysical methods based on resistivity were used to constrain the subsurface geometry of the feature (see further information and application in Salazar-Rincón et al., 2013; Turu et al., 2018). A vertical electric sounding followed by postprocessing using freely available IPI2win software from the University State of Moscow to solve equivalence problems and to invert the field data was performed using Bobachev et al. (2003) software. This data was combined with electrical resistivity tomography (Hausmann et al., 2013; Schrott & Sass, 2008). Geoelectric profiles were obtained using an 8-channel Agi Supersting system with dipole–dipole and Wenner–Schlumberger arrays and 1.5–2 m electrode spacing (Figure 3c; see Reynolds, 2011 for further information about the methods). Field data inversion with topographic correction was done using RES2DINV<sup>®</sup> (Loke et al., 2010). Topography was used to normalise profile elevations to the ground surface and for inversion best fit.

### 3.2.2 | Core sampling and magnetic susceptibility profiling

A borehole was performed from the topmost part of the landform for checking geophysical interpretations and chronological purposes. Multiple accessory equipment was necessary due to the grain-size variability of the deposits. The core was collected by adding the continuous sounding parts (Figure 3d), including PVC tubes, Russian-type corer and Wright piston corer (Wright et al., 1984).

Simple field identification of collected sediments (colour, texture and smell) helps to identify organic layers for  $^{14}\text{C}$  dating but also their sedimentary and thickness trend by identifying coarsening or fining upward sequences, thinning or thickening upward sequences (Jalut et al., 2010). Visual description and magnetic susceptibility measurements were done in situ shortly after collecting to identify unconformities and sedimentary units (Turu et al., 2018). A magnetic susceptibility measurement (MS) was carried out using a GF Instruments SM-20 shirt pocket-size magnetic susceptibility meter with a sensitivity of  $1 \times 10^{-6}$  SI units. To guarantee physical safety in the

transportation and storage identification of the cores, bivalve PVC casing, labelling and duct tape sealing were thereafter applied.

### 3.2.3 | $^{14}\text{C}$ AMS dating

Radiocarbon AMS dating from bulk organic fraction, charcoals and roots were performed in the sediment samples extracted from the bottom of the core. A pair of measurements of  $^{14}\text{C}$  activity and the isotope ratio  $^{13}\text{C}/^{12}\text{C}$  was done for each sample by Beta Analytic Inc. (Florida, USA) mass spectrometer facility. Possible biological contaminants (i.e., fungi) were avoided by drying the samples immediately after extraction and, subsequently, isolated into plastic bags. Samples were then stored at  $4^\circ\text{C}$  in a dry and dark place. The laboratory separates roots and other organic macro-remains from the bulk sediment. The organic matter was extracted from bulk sediment using the ABA protocol (acid–base–acid washing [HCl–NaOH–HCl]), to remove carbonates and possible humic acids. The resulting fraction was dried and prepared for dating following standard protocols (Walker, 2005). A couple of AMS measurements involving both macro-remains and bulk organic matter were executed to check their consistency (double AMS-data checking). The percent of modern  $^{14}\text{C}$  carbon (pMC) allows for a calibrated age using Reimer et al. (2020) datasets.

## 4 | RESULTS

### 4.1 | Surficial data

#### 4.1.1 | UAV high-resolution mapping

LiDAR DTM allowed the detailed description of the shape and size of the Calderueas hydrolaccolith and its surroundings. Table 1 and Figure 4 show the main characteristics of the structure. It is represented by an ellipsoidal morpho-structure trending NE–SO, 59 m long, 22.5 m wide and  $\sim 4$  m high. The central part of the hydrolaccolith presents its highest elevation in the E–NE part of the structure. In contrast, the lowest elevation is achieved in the W limit, leading to a total ground elevation difference of  $\sim 30$  cm. Its depth may vary from one

**TABLE 1** Main morphological parameters of the Calderuelas hydrolaccolith.

Main parameters	
Long axis	59 m
Short axis	22.5 m
Perimeter	170.07 m
Surface	2126 m <sup>2</sup>
Height	4 m
Internal volume 2010	3142.4383 m <sup>3</sup>
Internal volume difference February–July 2022	132.153 m <sup>3</sup>

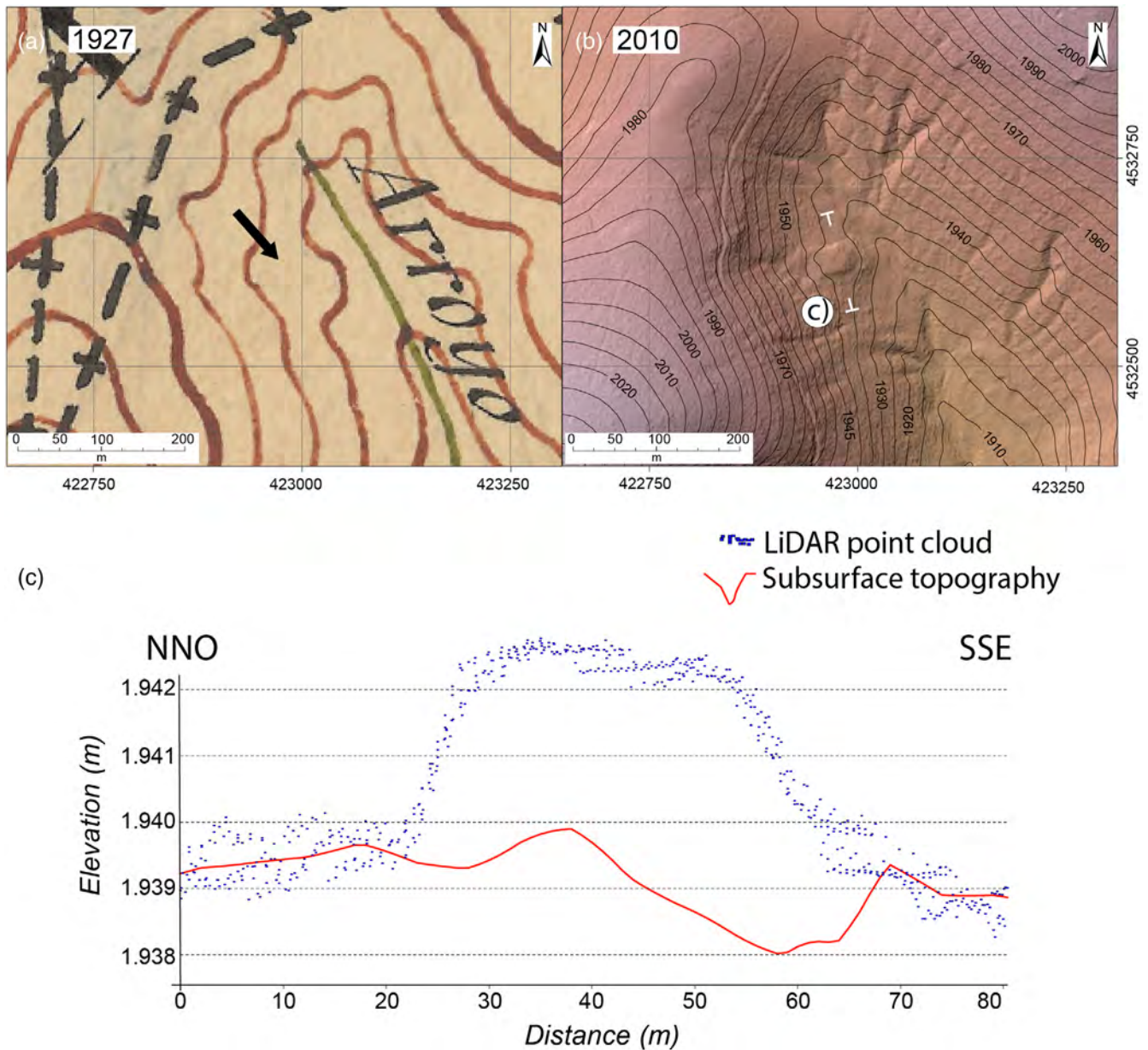


**FIGURE 4** (a) 1927 topographic map of the area (black arrow shows the position of the hydrolaccolith). (b) 2010 hypsometric map based on the LiDAR DTM marking the profile position shown in (c). (c) This work uses a 2D image of the frost mound structure based on LiDAR and geoelectric tomography (profile 1 in Figure 6a). ETR589 projection and UTM-T30 coordinate system. [Colour figure can be viewed at [wileyonlinelibrary.com](http://wileyonlinelibrary.com)]

sector to another, showing two throughs ~3 and ~4 m. The deepest is located towards the feature's eastern side.

Geomorphic evidence indicates the current active nature of the hydrolaccolith. It is important to notice the development of an associated drainage system, indicating the presence of sporadic streams in the area. However, it is most likely that these small scours were seasonal (see negative openness map in Figure 5a), as supported by the drainage system deflection observed in this area.

These geomorphological features were identified in the 1945–1946 aerial images, whilst the swelling surface was also recognised in the 1927 topographic map (Figure 3a). Another characteristic feature

is the presence of decametric dilatation scars observed at the frost mound foot. These fractures suggest that the creeping mechanism is still active today (Figures 5b–d and 6a).

So far, the processed LiDAR DTM maps (e.g., slope, principal components and sky view factor maps) show typical hummocky surfaces across the crest of the main feature. Most of its central part, especially towards the east, is uplifted, whilst the western side appears depressed. Maximum surface elevation occurs on the northern border of the structure, where seasonal ice lenses were observed. This terrain configuration is consistent with the surface changes observed in the February–July subtraction DSM map derived from UAV images

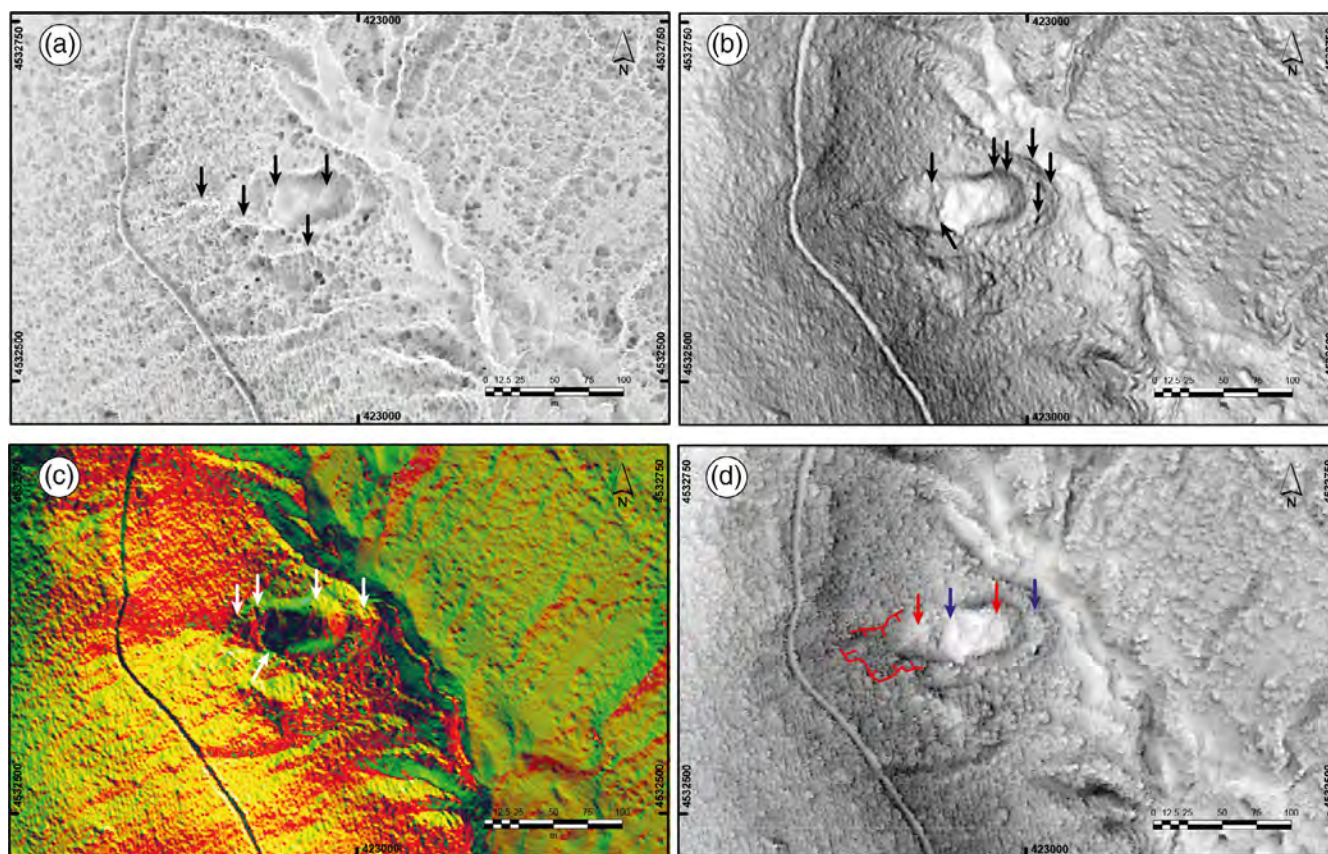


**FIGURE 5** Microrelief analysis: (a) Negative openness map showing the drainage system affecting the main structure (see black arrows). (b, c) Slope and principal components map indicating the scars and depressions affecting the hydrolacololith structure, respectively (see black arrows). Colours correspond to the RGB composition band values considering three components for PCA using a hill-shading searching radius of 16 directions and 35° sun elevation. (d) Sky view factor map. Arrows mark the position of positive (red) and negative (blue) topography, and red lines show the position of the source area of the mass movement. Based on 2010 LiDAR data ([www.ign.es](http://www.ign.es)). [Colour figure can be viewed at [wileyonlinelibrary.com](http://wileyonlinelibrary.com)]

(Figure 6b). Moreover, the aerial photointerpretation from different periods shows significant drainage pattern changes within the frost mound (Figure 7).

#### 4.1.2 | Surficial temperature measurements

Preliminary thermal measurements at 10 cm depth were systematically carried out during the winter (February) and summer (July) of 2022. The winter ground surface temperature varies between  $-7.9$  and  $6.7^{\circ}\text{C}$  (mean =  $-0.6^{\circ}\text{C}$ ). In situ observations have shown the existence of thick ice interstitial wedges standing out in different sectors of the hydrolacololith (Figure 8a–d), whilst a ground thermal range between  $3$  and  $11^{\circ}\text{C}$  was observed in the summer (mean =  $7^{\circ}\text{C}$ ). Although the number of measurements (1 year) provides a first-order assessment of the local ground thermal regime, the mean annual ground thermal oscillation reaches  $7.6^{\circ}\text{C}$ .

The 2D Fourier surface thermal map (data obtained in July) showed two important distributed anomalies with a 30-m long wavelength (minimum at  $3.8^{\circ}\text{C}$  and maximum at  $11.4^{\circ}\text{C}$ ) across the feature.

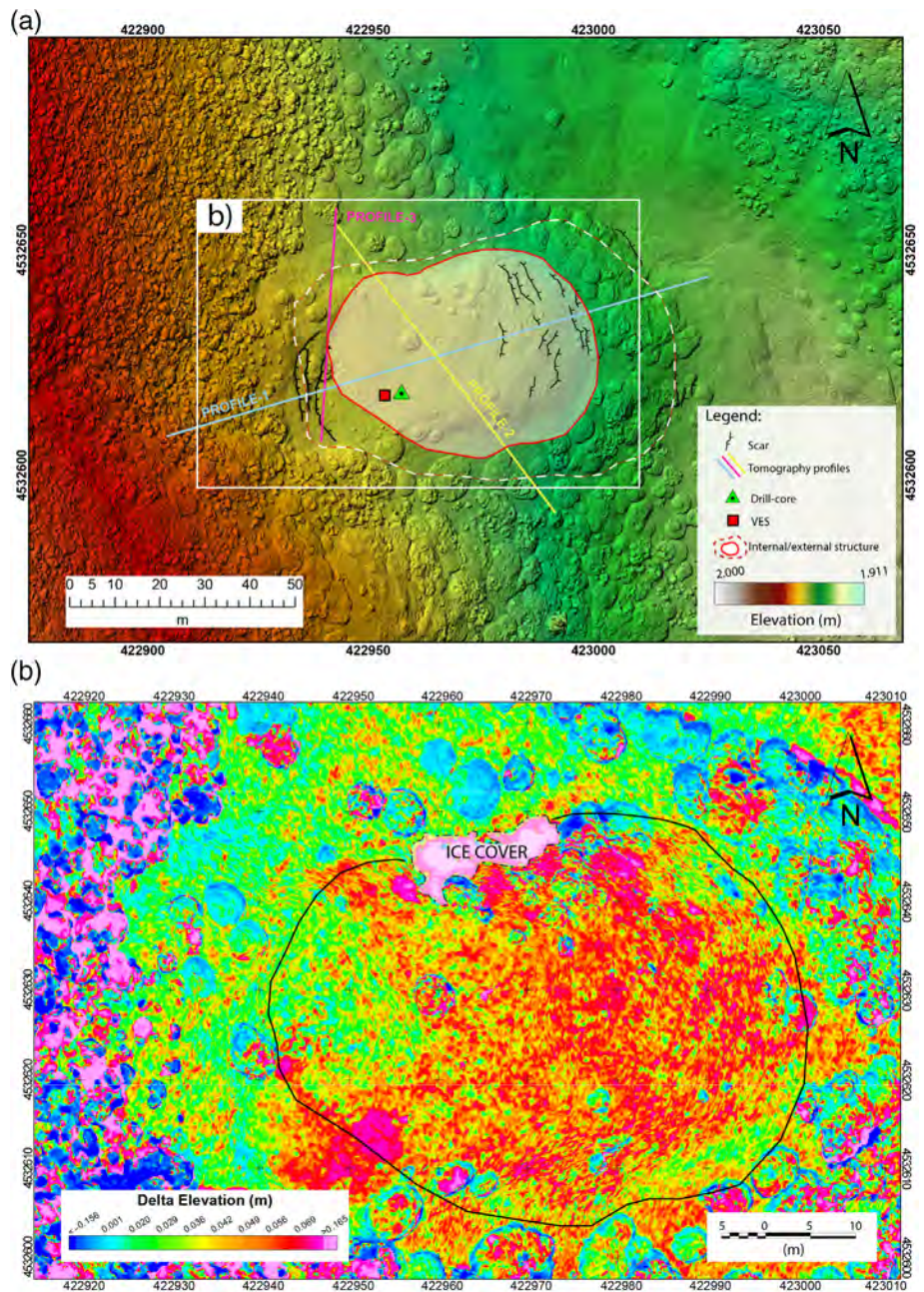
The lowest values were reached in a localised depression of the western sector, whereas higher values were recorded in the elevated areas of the eastern sector of the structure, showing an N–S strike (Figure 9).

## 4.2 | Subsurface data

### 4.2.1 | Geoelectric surveying

Three geoelectric profiles were measured with varying lengths from 48 to 137 m. The maximum depth achieved was over 10 and 24 m using Wenner and dipole–dipole arrays, respectively. Geophysical data show three different resistivity units (G1, G2 and G3, Figure 10a). The upper unit (G1: 2.5–5 m thick) is characterised by low resistivity, being interpreted as a surficial formation with high content in fine-grain material. The intermediate unit (G2: 5–7 m thick) seems to comprise variable content of fine grain material interpreted as part of the mass flow deposit. Its core shows higher resistivity than the surroundings (G2a >  $8000\ \Omega\text{m}$  and G2b  $\approx 3000\ \Omega\text{m}$ ). The lower

**FIGURE 6** (a) UAV-derived DSM with the position of the geoelectric tomography profiles and drill core. The map shows the internal/external structure of the Calderuelas hydrolaccolith and the main scars observed from the DSM. (b) Subtraction topographic map showing seasonal vertical ground changes observed between February and July 2022. The black line indicates the internal area of the hydrolaccolith shown in (a). [Colour figure can be viewed at [wileyonlinelibrary.com](http://wileyonlinelibrary.com)]



unit (G3) was interpreted as bedrock having a much lower resistivity than the previous unit ( $G3 \ll G2$ ).

The comparison of the three units suggests an inverse relationship between units G1 and G2 (Figure 10a), which also correlates with a topographic height in the centre of the structure. This concentric differentiation of the three resistivity units allows the peripheral delimitation of the active zone of the hydrolaccolith. The general geometry of the bottom shows a basin-like morphology varying the depth between 3.5 and 4 m.

A single vertical electrical sounding (VES) was performed in winter on the summit of the landform, obtaining a 1D resistivity profile at the same place where a 2D resistivity panel was produced in summer to compare both resistivity data (Figure 10b). The resistivity from VES

shows the same layered structure (Table 2) obtained with tomography in summer; however, resistivity differences for summer (electrical resistivity tomography, ERT) and winter (VES) can be found in Figure 10b. Unit G1 in winter has a resistivity of 20% higher than in summer, but a greater resistive difference is for Unit G2. Two possibilities arise for electrical resistivity changes: void ratio increasing (dilatation), the presence of ice in the soil, or a frozen layer in winter. The last possibility is likely for Unit G3; however, this is not possible within Unit G2 due to the swelling capacity of the fine-grain material, for which we invoke dilatation as a potential phenomenon to explain the signal. Therefore, the morphology seems to be controlled by the presence of groundwater, a freeze shallow water table within the first metre of Unit G1 and a piezometric water level within Unit G2.

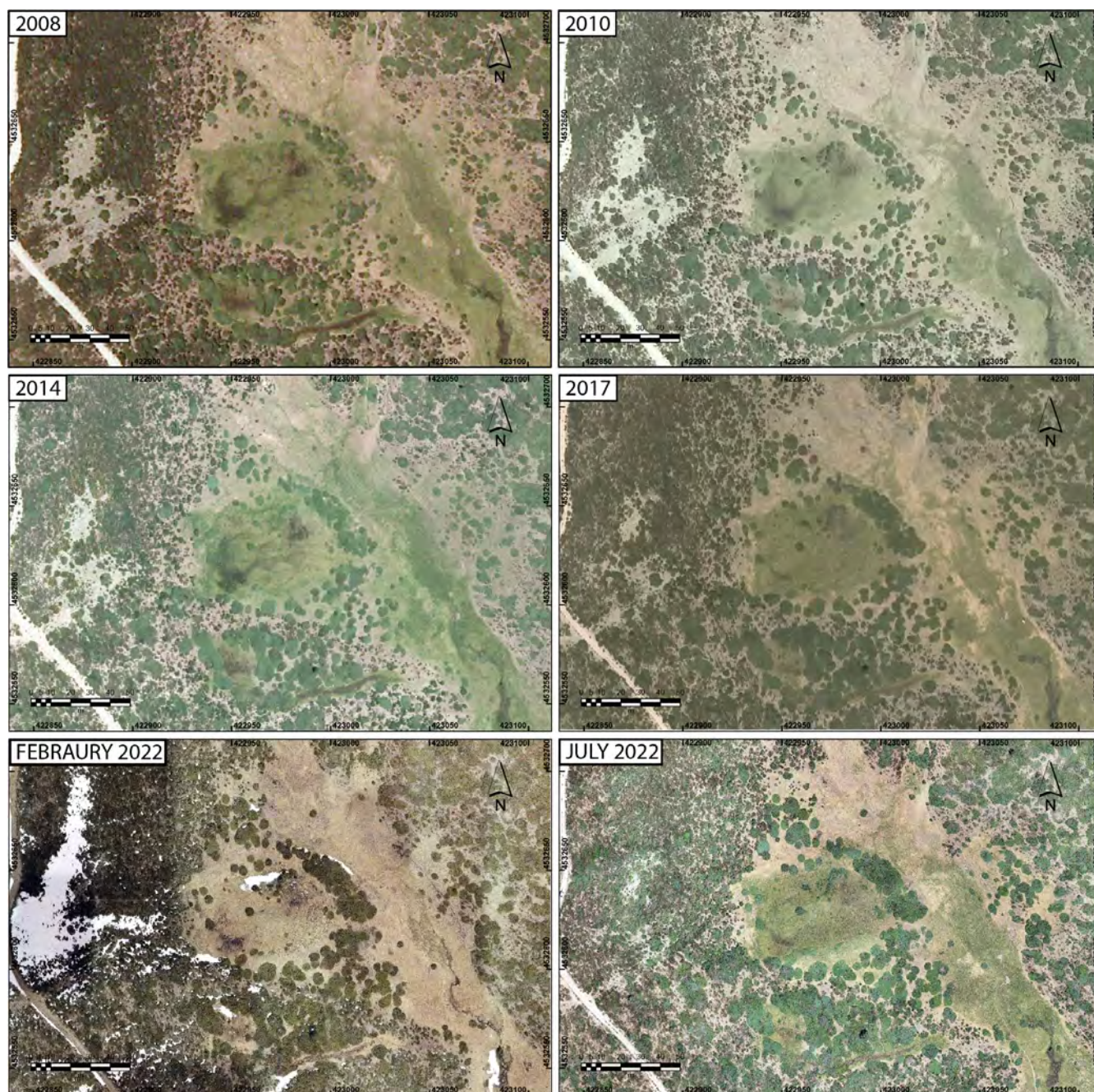


**FIGURE 7** Time series orthoimages from PNOA (2008, 2010, 2014 and 2017) and flights carried out in 2022, where changes in the internal drainage system can be identified clearly, suggesting the presence of flooded sectors within the frost mound. [Colour figure can be viewed at [wileyonlinelibrary.com](https://onlinelibrary.wiley.com/doi/10.1002/ldr.4968)]

#### 4.2.2 | Core sampling and magnetic susceptibility profiling

A 374 cm continuous sediment core was extracted from the top of the Calderuelas hydrolaccolith, spanning the upper geoelectrical unit (G1). The upper 50 cm were extracted with a 76 mm PVC tube, hammering directly into the surface of the feature. The segment spanning between 50 and 150 cm in depth was collected with a Russian-type corer. A Wright piston corer obtained sediment between 150 and 300 cm in

depth. The last 66 cm were retrieved with an auger. The presence of gravel and pebbles impedes reaching a greater depth than 374 cm. The precise description of the sedimentary units is depicted in Figure 11.

MS measurements indicate that low values were related to the most organic sections of the borehole, whilst high MS values were found at the bottom of the sounding, where inorganic sections of abundant pebbles and graves were found. At least four MS changes at  $\sim 20$ ,  $\sim 140$ ,  $\sim 220$  and  $\sim 374$  cm coincide with sharp grain-size changes that are interpreted as sedimentary boundaries (Figure 11b).



**FIGURE 8** (a) General overview of the hydrolaccolith during winter 2022. (b, c) Detailed image of ice sheets growing over the surface. (d) Subsurface interstitial ice. [Colour figure can be viewed at [wileyonlinelibrary.com](http://wileyonlinelibrary.com)]

#### 4.2.3 | $^{14}\text{C}$ AMS dating

Two samples were collected from the bottom of the sounding at 306–326 cm depth (GU-C09-1) and 374–366 cm depth (GU-C10-1). Four AMS  $^{14}\text{C}$  determinations were carried out: two from bulk sediment, one from charred remains (charcoal) and one from organic macro-remains (roots or plant remains; Figure 12). Unfortunately, only the sample collected at 306–326 cm depth had enough charred remains to produce reliable AMS  $^{14}\text{C}$  data. Table 3 shows the data of the three AMS  $^{14}\text{C}$  produced using the core samples. GU-C09-1 yields a calibrated  $^{14}\text{C}$  at  $2\sigma$  of 4419–4244 years BP (BP = related to 1950), and the GU-C10-1 affords an age of 2326–2144 years BP. The results provided close maximum limiting ages for Unit G1 and minimum limiting ages for units G2 and G3 (Table 3). However, the inverted age from the bottom of the core was over by doubling the AMS measurements (see Appendix S1 for a detailed description of the AMS  $^{14}\text{C}$  double-date checking), ranging  $7076 \pm 2832$  yrs cal BP for unit G2.

## 5 | DISCUSSION

### 5.1 | Driving mechanism

Altogether, including geophysical and sedimentary records, we interpret that the primary process responsible for the swelling was a mass

movement, potentially paraglacial in origin, that mobilised the units G1 and G2 downslope (Stage 1). According to the sediment core, below the fine-grain soil and solifluction deposits (G1), the G2 unit is predominantly composed of grain-size sediments, including peat soils and rounded-to-angular gravels that we infer act as a subsurface drainage layer. The G2 unit is, therefore, constrained by impermeable bedrock (G3). This internal structure would give rise to swelling by facilitating hydration and dilatation/contraction during freeze–thaw cycles (Figure 13).

During intervals of relatively cold temperatures (Stage 2), shallow frost penetration produces hydrostatic overpressure in unit G2 unit, affecting subsurface drainage and promoting the accumulation of fine grain sediments at the slope-floor transition of the valley. Further cooling (Stage 3) allows deeper frost penetration, further enhancing hydrostatic pressure over the G2 unit. Furthermore, given that solar radiation exhibits a differential effect on the valleys, it is likely that the frost penetration would reach more depth at the floor of the valley, creating a “thermal barrier” that traps the drainage and increases hydrostatic pressure on the transition between the slope and the bottom of the valley. The invoked “thermal barrier” might be represented in our geophysical record as the lateral high electrical resistive unit (G2a in Figure 10a) located at the snout of the landform, a frosted snout. Thus, once drainage within the landform is blocked by the frosted snout, the hydrostatic pressure cumulates and may push up

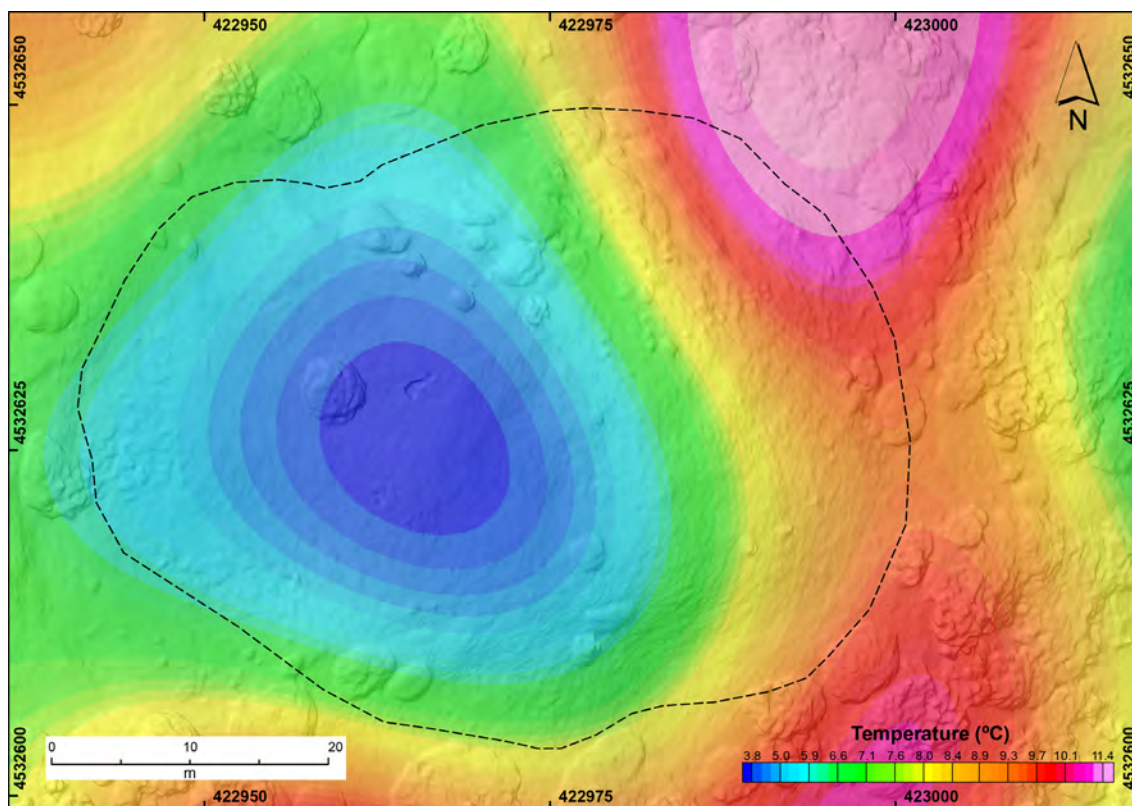


**FIGURE 9** Result of the 2D-Fourier analysis of thermal gradient filtered to show large wavelength anomalies. The map marks the position of positive and negative thermal anomalies. Dashed lines illustrate the position of the internal part of the Calderuelas hydrolaccolith. [Colour figure can be viewed at [wileyonlinelibrary.com](https://onlinelibrary.wiley.com/doi/10.1002/ldr.4968)]

the impermeable fine grain-size lenses, generating deformation on G1, the upper layer and, therefore, the maximum swelling of the feature. It is also likely that surficial expansion cracks formed during this stage because of horizontal creeping (Figure 6a). Finally, the onset of warm temperatures (Stage 4) led to the disappearance of the ground frost, decreasing the hydrostatic pressure over unit G2. This configuration allows the free movement of subsurface water towards the valley floor and the accumulation of fine-grain sediments under the hydrolaccolith (Figure 13).

The invoked swelling process at Calderuelas Valley involved a series of factors that associate this structure genetically with an external hydrological system affected by ground freeze–thaw annual cycles (Figure 13). According to the classification by Washburn (1979), the Calderuelas hydrolaccolith may correspond to a palsa typology or frozen peat mounds (Fewster et al., 2020; Kirpotin et al., 2011; Olvmo et al., 2020). Although, other studies suggest that palsas can occur without positive hydrostatic pressure (i.e., independent of external water supply) (Cummings & Pollard, 1989; Pollard & French, 1984; Seppälä, 1986). Conversely, pingos are often isolated structures that present larger dimensions with water left over (i.e., hydrostatic pingos or closed systems) (Kunz & Kneisel, 2021) or related to positive hydrostatic strain (i.e., hydrodynamic pingos or open systems) (Mackay, 1972, 1979; Ross, 2013). Remnants of fossil pingos have also been described in Northern Europe (Pissart, 1994), far from the

present-day permafrost areas, suggesting that they may have formed after the last glacial event. Examples in Wales, France and Belgium have shown close similarities with the Calderuelas frost mound being found in gentle slopes and subhorizontal plateaus but with larger dimensions (150 × 250 m). Despite some authors dissuading its use, the term hydrolaccolith is frequently used as a synonym for hydrodynamic pingo-like structure because of the essentially external hydrodynamic control and ubiquitous emplacement in a wide range of periglacial environments (Ward, 2004; Woolderink, 2014). The data collected in this study agree well with the hydrodynamic pingo-like structure definition, so the Calderuelas hydrolaccolith might be classified as such.

The timing of the genesis of the Calderuelas pingo-like is puzzling because of the inverted  $^{14}\text{C}$  ages obtained from the bottommost segment of the sediment collected (Table 3). The lowest ages, which are anomalously young, correspond to the basal unit, mainly composed of inorganic sands, gravels and pebbles, with a reduced amount of organic matter that may provide poor radiocarbon results. An additional possibility to explain inverted ages is contamination from the upper part of the borehole due to the auger coring system. Finally, percolation processes mixing different sources of radiocarbon in a sedimentary landform likely experiencing strong variations in the subsurface water levels cannot be discarded either. Although the chronological data indicate that the Calderuelas pingo-like

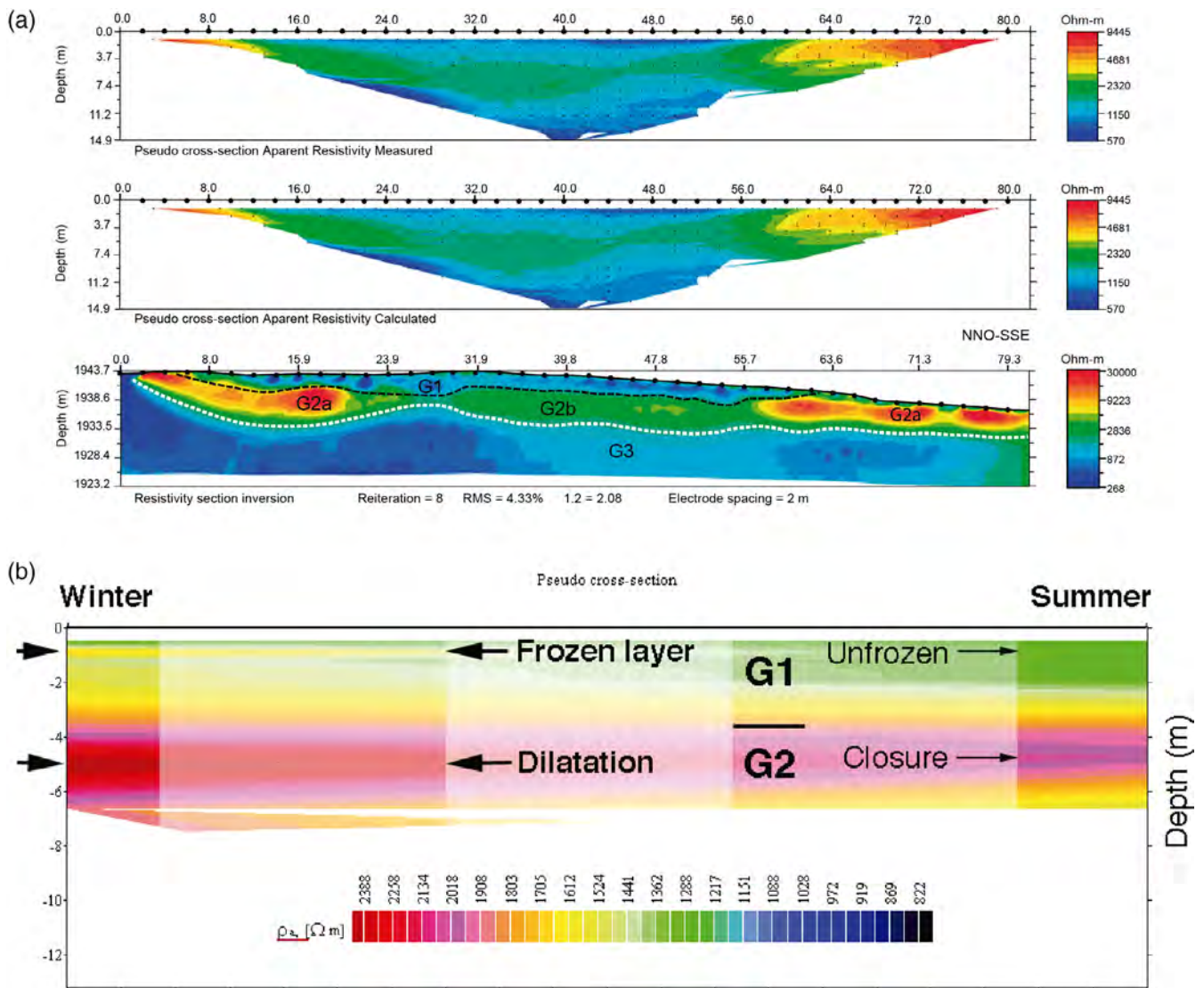


**FIGURE 10** (a) 2D-Geoelectric tomography profile showing different resistivity units. See the text for an explanation of the interpretation. (b) Resistivity differences between winter and summer within the first 8 m depth. Two resistive layers emerge in winter at 1 m depth inside the resistive unit G1 and 4.5–5 m depth inside the resistive unit G2. [Colour figure can be viewed at [wileyonlinelibrary.com](http://wileyonlinelibrary.com)]

**TABLE 2** Inverted resistivity model in 1D from winter using VES procedure.

Layer	Mean resistivity (Ohm m)	Depth (cm)
G1	1356	394
G2	7375	738
G3	167	>738

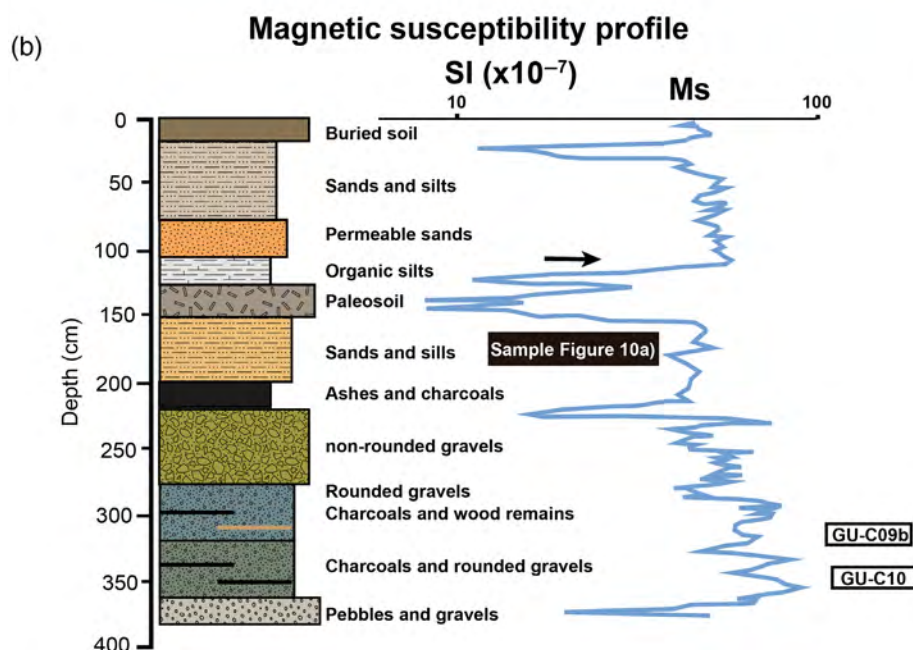
structure started its activity sometime between  $\sim 4.3 \pm 0.1$  and  $\sim 2.2 \pm 0.1$  cal ka BP, we favour the  $^{14}\text{C}$  data collected from the core segment spanning between 306 and 326 cm (i.e., GU-C09-1) and interpret it as a close minimum limiting age for the formation of the feature. If correct, the data supports mid-Holocene climate-driven activity for the Calderuelas pingo-like structure, most likely since  $\sim 4.3 \pm 0.1$  cal ka BP (Table 3).

## 5.2 | Middle to late Holocene environmental and climatic evolution

Based on cosmogenic-derived chronological data, it is widely accepted that glaciers in Sierra de Guadarrama disappeared during the transition between the Late Glacial and the early Holocene around 10 ka (Marcos et al., 2022; Oliva et al., 2019; Palacios et al., 2012). However, one  $^{10}\text{Be}$  age obtained from the innermost moraine reported in the Hoyo Grande valley, located a few km to the north of the study site, indicates ice advance culmination at  $4.3 \pm 0.3$  ka BP (Carrasco et al., 2016). Although preliminary, this age suggests that local deglaciation, or at least the cessation of glacial-prone conditions, could occur coevally with the Calderuelas hydrolaccolith's activity during the mid-Holocene. This is consistent with the prior interpretation of a paraglacial origin of the landslide that promoted the subsequent formation of the Calderuelas pingo-like feature (Figure 13).



**FIGURE 11** (a) Core sample section from 1.5 to 1.9 m depth. (b) Stratigraphic section based on the core sample and magnetic susceptibility data. Magnetic susceptibility profile from unit G1. Dated samples are labelled as GU-C09b and GU-C10. Pebbles and gravel from the bottom of the borehole can be related to the upper part of Unit G2. A facies-rich sedimentary sequence is within unit G3, ranging from rounded gravels to buried soils, palaeosoils, peat and layers containing ashes and charcoals. [Colour figure can be viewed at [wileyonlinelibrary.com](https://onlinelibrary.wiley.com)]



However, one  $^{10}\text{Be}$  age obtained from the innermost moraine reported in the Hoyo Grande valley, located a few kilometres to the north of the study site, indicates ice advance culmination at  $4.3 \pm 0.3$  ka BP (Carrasco et al., 2016).

At the local-to-regional scale, palynological analysis conducted on the Guadarrama mountains reveals a marked decline in arboreal pollen starting at  $\sim 4.1$  cal ka BP (Franco-Múgica et al., 1998) occurring within a widespread multimillennial aridification trend across Iberia beginning at  $\sim 5.5$  ka (Morales-Molino et al., 2013; Turu et al., 2021). This climate pattern also coincides with the innermost moraine built-up at Hoyo Grande (Carrasco et al., 2016), a mid-Holocene neoglacial episode in the northern slope of the Pyrenees (Cirque de Troumouse; Gellatly et al., 1992) and the eustatic sea level fall across the Iberian margins between  $\approx 6.0$  and 3.8 ka (Hernández-Molina et al., 1994). At the hemispheric scale, the

appearance of the Calderuelas hydrolaccolith is contemporaneous with the onset of the so-called 4.2 ka Event, which has been generally associated with intense droughts and colder conditions around the Mediterranean basin (Bini et al., 2019) occurring each  $4.5 \pm 0.5$  ka (Hernández-Molina et al., 1994; Turu, 2023; Turu et al., 2023). The chronology of these long-range climate oscillations is in line with the formation of the Calderuelas hydrolaccolith, and, therefore, we interpret that the latter occurred under progressively drier conditions and slightly colder temperatures potentially enhanced by local topoclimatic factors.

The data collected in this study also allows inferences regarding the current environmental and climate controls driving the dynamics of the Calderuelas hydrolaccolith. The present-day activity of the landform is assessed regarding UAV-derived and surface/subsurface (10 cm depth) thermal data.

**FIGURE 12** (a) Bulk organic fraction from 374 to 366 cm depth, sample GU-C10-1(H). Millimetre grid (photography from Beta Analytic,  $\beta$ -636432). (b) Plant remains from 374 to 366 cm depth, sample GU-C10-1(H). Millimetre grid (photography from Beta Analytic,  $\beta$ -638078). (c) Bulk organic fraction from 306 to 326 cm depth, sample GU-C09b-1(H). Millimetre grid (photography from Beta Analytic,  $\beta$ -636433). (d) Charred remains from 306 to 326 cm depth, sample GU-C09b-1(H). Millimetre grid (photography from Beta Analytic,  $\beta$ -639097). [Colour figure can be viewed at [wileyonlinelibrary.com](http://wileyonlinelibrary.com)]

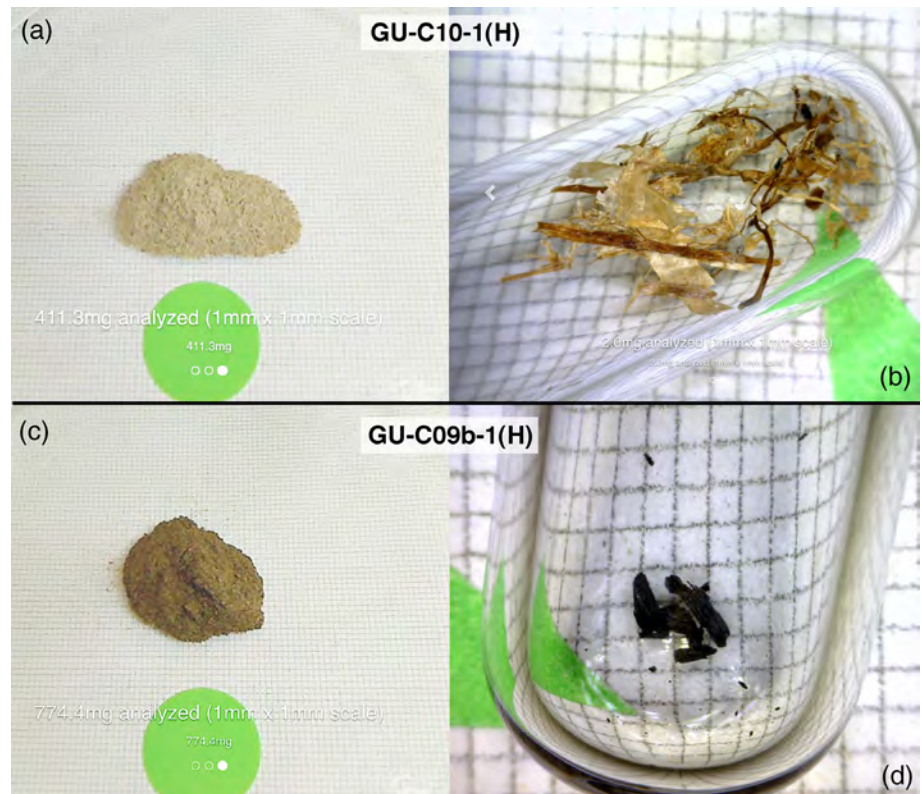


**TABLE 3** AMS determination results and cal BP from INTCAL20, and cal BP ages from INTCAL13 (+NHZ1).

Sample	Laboratory	Depth	pMC	Years BP	Years cal BP	$\delta^{13}\text{C}$
GU-C09-1(H)	$\beta$ -636433 (bulk)	306–326	$61.42 \pm 0.23$	$3910 \pm 30$	4419 to 4244	$-25 \pm 0.1\%$
GU-C10-1(H)	$\beta$ -636432 (bulk)	374–366	$75.95 \pm 0.28$	$2210 \pm 30$	2326 to 2144	$-26.2 \pm 0.1\%$
	$\beta$ -638078 (plant)		$119.19 \pm 0.45$	$-1410 \pm 30$	-34 to -37	$-26.6 \pm 0.1\%$

The spatial distribution of the documented seasonal variations (February–July) in height and length broadly coincides with the outlined thermal anomaly map. The ground thermal variation between  $-0.6$  and  $7^\circ\text{C}$  observed in the study site matches well with 10-year direct measurements from the nearby Peñalara Massif ( $\sim 2000$  m a.s.l.), which ranges between  $\sim 0^\circ\text{C}$  in February and  $15.95^\circ\text{C}$  in July at 10 cm depth (Palomo-Segovia, 2012), particularly during the coldest month. These values were obtained in situ, although the freeze conditions affected the hydrolaccolith as supported by the presence of interstitial ice lenses observed during the winter period (see Supplementary material). Additionally, a strong linkage between air temperature and surface/subsurface ground temperatures between June and December has been reported in the same spots (Palomo-Segovia, 2012). A climate control dominated by annual temperature oscillations is invoked to explain the current dynamics of the Calderuelas hydrolaccolith. So, it is most likely that vertical variations in the hydrolaccolith are mostly governed by freeze–thaw cycles, whereas horizontal development is driven by creeping processes derived from swelling. These active stages of the feature probably reach their maximum activity between the fall (October) and early winter (December)

before the onset of the seasonal snow cover, which decouples air and ground temperatures as reported in the Peñalara Massif (Palomo-Segovia, 2012).

Seasonal water pools were found on the western limit of the structure, mostly coinciding with the smaller thermal anomaly, whereas the eastern portion is characterised by a thermal high, which might indicate the absence of water underneath and the presence of a levee front (Figure 9). The presence of a shallow water table is associated with the growth of ice lenses during the fall–winter period and markedly surface deformation (Figure 8). The heterogeneous presence of seasonal water pools can explain the detected differences in the uplifting response during the annual evolution of the hydrolaccolith by controlling surface/subsurface temperatures (Figure 6b).

Overall, the observed surface/subsurface thermal variations in the Calderuelas hydrolaccolith are most likely promoted by the tight relationships between meteorological variables along with topography, geomorphology, edaphic and biogeographic factors that affect soil temperatures and, therefore, influence the typical processes occurring across mountain landscapes (Andrés-de Pablo & Palacios-Estremera, 2010; Palomo-Segovia, 2012). For instance, the genetic/

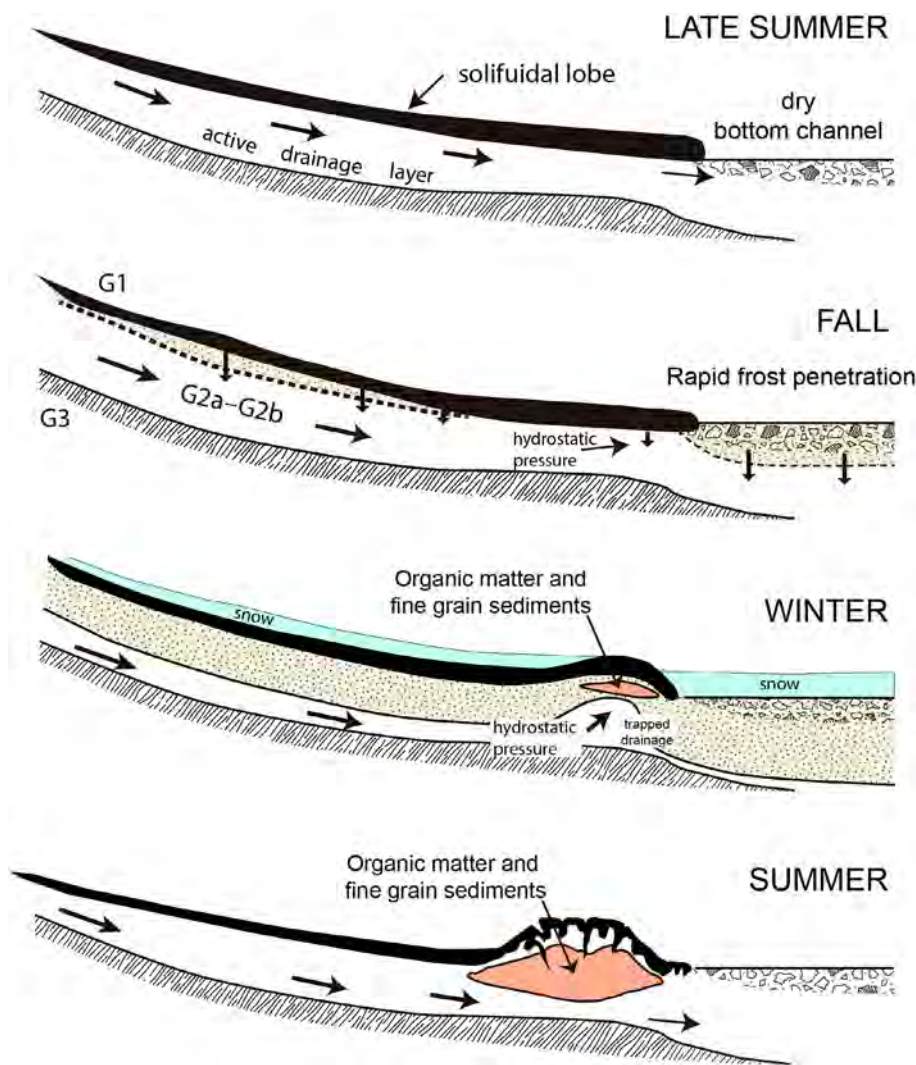


**FIGURE 13** Genetic and evolutive model of the Calderuelas hydrolaccolith. Modified from Ballantyne and Harris (1994). G1, G2 and G3 are the layers identified in the geoelectric tomography (see Figure 10). [Colour figure can be viewed at [wileyonlinelibrary.com](http://wileyonlinelibrary.com)]

evolutive model proposed considers the hillside orientation as a crucial driver in the Calderuelas Valley ground thermal regime partly due to its modulation of incoming solar radiation, air temperature and snow cover duration (Melón-Nava et al., 2022). Although these variables seem to play a key role in local seasonal ground thermal conductivity in the Calderuelas Valley, a long-lasting monitoring programme is needed to understand further the annual thermal regime of such periglacial landform (Groos et al., 2022; Marcos & Palacios, 2004; Palacios et al., 2003; Serrano et al., 2020; Vieira et al., 2003).

### 5.3 | Comparison with other Iberian frost mound features

Little is known about frost mounds across the Spanish Central System (~41°N). Pedraza (1987) reported analogous frost mounds accompanied by polygonal grounds in the Sierra de Guadarrama at similar altitudes and topoclimatic conditions to the Calderuelas hydrolaccolith.

However, these landforms were smaller in size and currently inactive (1–3 m in diameter).

Some typologies of frost mounds have been reported across the Iberian Peninsula, most of them located on the northernmost mountain ranges (Oliva et al., 2018; Serrano et al., 2019). In the central Pyrenees (~43°N), Serrano et al. (2019) document the existence of active frost mounds ranging 1–3 m in diameter up to 2670 m a.s.l. starting at the so-called middle periglacial belt and continuing across the supra-periglacial belt, up to 2900 m a.s.l. The morphodynamics of the lower features were primarily associated with the frozen soil regimes and snow cover, whereas the highest frost mound evolution was directly linked to the presence of permafrost scarcely modulated by local topoclimatic factors (Serrano et al., 2019).

In the Picos de Europa range (~43°N) located in the Cantabrian Mountains, Serrano et al. (2018) report the presence of active frost mounds around 1 m in diameter up to 1900 m a.s.l. In this case, frost mounds have been associated with debris covering relict ice patches, so their morphodynamics is primarily controlled by variations in the seasonally frozen ground and nivation processes.

In southern Iberia, specifically in the Sierra Nevada mountains ( $\sim 37^\circ\text{N}$ ), the existence of frost mounds is still unknown despite their high altitude and prevailing periglacial conditions above 2500 m a.s.l. (Oliva et al., 2018; Serrano et al., 2018).

Overall, the Calderuelas pingo-like feature differs from other analogous periglacial landforms across Iberian mountains in four key aspects: size, morphodynamics, age of formation and present-day climate conditions. First, the Calderuelas hydrolaccolith is significantly larger, reaching 59 and 22.5 m along its axis, in contrast to other frost mounds reported in the Pyrenees and Picos de Europa of 1–3 m in diameter (Serrano et al., 2018, 2019). Second, generally, frost mounds in northern Iberia have been associated with the presence of permafrost and/or relict ice lenses, whereas the Calderuelas hydrolaccolith is directly linked to the frozen ground regime and external subsurface drainage. Third, all the northern frost mounds developed within the limits of areas previously glaciated during the Little Ice Age (LIA; Serrano et al., 2018), suggesting that their formation occurred within the last centuries (Oliva et al., 2016, 2018). In contrast, radiocarbon ages suggest that the Calderuelas hydrolaccolith's activity started at least at  $\sim 4.3 \pm 0.1$  cal ka BP and, thus, the upper layer over which the periglacial activity develops dates back to the mid-Holocene. To the west of the Iberian Central System, a temperature lowering of almost  $1^\circ\text{C}$  is computed at event 4.2 in the Navamuño peatland (Turu et al., 2021). Nowadays, Serrano et al. (2019) report mean annual temperatures of the air and the ground between 2670 and 2900 m a.s.l. in the central Pyrenees spanning  $2.5^\circ$ – $0.5^\circ\text{C}$  and  $3^\circ$ – $2^\circ\text{C}$ , respectively, whereas the nearby Peñalara Massif in the Central System exhibits significant warmer annual air and ground temperatures of  $7^\circ$ – $0.6^\circ\text{C}$ , respectively at 1800 m a.s.l. Altogether, our findings suggest that the Calderuelas hydrolaccolith could be the largest, older, warmest and southernmost periglacial landform controlled by the seasonally frozen ground regime of its type in Iberia.

## 5.4 | Integration of top-to-bottom methodologies

The introduction of geomatic technologies such as LiDAR and UAVs opens a broad field of glacial and periglacial landform study. Recent advances in the study of geomorphological processes have implemented terrestrial laser scanning and airborne laser technologies (LiDAR or ALS) to estimate terrain changes in periglacial environments, such as analysis of rock glacier evolution (Robson et al., 2022), detection of polygon networks (Beerten et al., 2021), and exploration and monitoring of solifluction processes in alpine landscapes (Holst et al., 2021). The acquisition of DEMs provides the basis for further numerical modelling (Abolt et al., 2017) and remote sensing applications necessary for the detailed characterisation and mapping of different features (Colucci et al., 2016; Haugerud et al., 2003; Hopkinson & Demuth, 2006; Jónsson et al., 2014). Characterisation and detection of frost mounds using LiDAR data gave good results in other regions where these structures are perennial, such as in the arctic regions (Jones et al., 2013; Luo et al., 2019), but it is a relatively novel

technique on low-latitudes mountain environments such as the Spanish Central System (see Serrano et al., 2018 and references therein).

Amongst the main gains of this technology is the possibility to rapidly explore remote areas with a dense vegetation cover, obtaining high-resolution DEMs suitable for detailed mapping. However, point clouds derived from surface scanning only give information about the ground surface, and the postprocessing stage requires further powerful computer work to assess the acquired datasets properly. Although most of the National Administrations provide free access to their LiDAR datasets, the availability of high-resolution datasets does not always fulfil the needs of geomorphologists, especially when monitoring certain processes that require several flights per year. Fernández-Lozano and Gutiérrez-Alonso (2016) have demonstrated that resolution can be improved by postprocessing LiDAR data with visual enhancement tools, providing successful results to explore landscape micromorphologies. Although different algorithms have often been of interest in archaeological works (Doneus, 2013; Fernández-Lozano & Gutiérrez-Alonso, 2016; Kokalj et al., 2011; Zakšek et al., 2011), this methodological approach has also been adapted for the geomorphological analysis of glacial and other landforms with great success (Carrasco et al., 2020; Prima & Yoshida, 2010). However, the application of this technology to study a frost mound is relatively new. De la Barreda-Bautista et al. (2022) described its use for monitoring palsa area degradation and the existing variations when comparing it with other remote sensing methods like InSAR. In their study, these authors suggest that UAV data can improve the dynamics assessment of such landforms at a local scale. Other research has also shown that the identification and analysis of periglacial landforms by integrating multiple remote sensing technologies can offer key upgrades for analysis (Luo et al., 2019). All these previous works did not use RTK-UAVs, which forced them to provide ground control points during each flight to increase high precision and accuracy during the processing of photogrammetry data. This is a time-consuming task and certainly difficult to accomplish in rough high mountain areas where frost mounds and other periglacial landforms develop. Our study demonstrates that data acquisition can be rapidly and accurately performed, saving time and resources using an RTK-UAV since postprocessing is much easier and faster than traditional topographic GNSS transformations.

## 6 | CONCLUSIONS

Unlike other described frost mounds in the Spanish Central System, the Calderuelas feature, located in the Guadarrama National Park, is characterised by its major dimensions and millennial prevalence. Its main morphological characteristics and dynamics, along with the presence of external hydrodynamics, can be linked with pingo-type structures. The origin of this feature is associated initially with a mass movement and derived from solifluction. This is supported by the geoelectric profiling, which showed a three-layer system comprising an upper of relatively impermeable sediments layer (G1); an intermediate layer of gravels and pebbles (G2) representing an aquiclude system

related to the mass movement, and a bottom layer (G3) comprising bedrock outcrops. According to these data, we invoked a swelling process affecting the structure related to the internal hydrostatic pressure and seasonal freeze-thaw episodes responsible for the geometric changes, as it is the current process affecting the landform. Electrical resistivity, in combination with analysis of different ortho-image periods, allowed us to identify the internal structure and the groundwater path fed seasonally with water under pressure in the aquiclude system. This process is invoked to be responsible for the topographic swelling. According to radiocarbon ages, the activity of the Calderuelas pingo-like feature started during the mid-Holocene at ca. 4300 years cal BP, maybe after the demise of permanent ice bodies that occupied the valley. Monitoring this type of structure using geomatic technologies successfully improves the analysis of the geometric changes. However, we are aware that a comprehensive assessment of controlling factors affecting the development of the hydrolaccolith requires long-time datasets, yet we consider that our study yields sufficient data to propose a conceptual model about its genesis and fundamental behaviour. LiDAR and UAVs are adequate technologies in accuracy and resolution for the study and description of surface changes, whilst geophysical techniques and shallow vertical soundings provide key insight for interpreting subsurficial variations. In addition, thermal monitoring is of great interest in controlling the behaviour and establishing the mechanisms that govern the evolution of these landforms. However, it requires large time windows for detailed analysis of the freezing-thaw processes related to the periglacial activity. Further research will allow us to analyse the seasonal thermal regime of the ground in the area. All in all, the multidisciplinary approach shown in this work allows for gaining insights into the top-to-bottom characterisation of frost mounds worldwide. This scientific information will help to improve the knowledge about its genesis and future evolution. Therefore, to guarantee the preservation of these landforms, which are strongly sensitive to climate changes and anthropogenic impacts, more detailed information about their rise and growth must be determined, adapting the management plans to facilitate their future preservation and public awareness.

#### ACKNOWLEDGEMENTS

This work was supported by the Spanish Ministry of Science and Innovation (FINICES, PID2020-117685GB-I00) and Castilla La Mancha University Research Group (UCLM, project 2023-GRIN-34112). The authors also wish to acknowledge the help and assistance of the Sierra de Guadarrama National Park Research Centre. VT acknowledges the Andorran Marcel Chevalier Earth Science Foundation for its financial support.

#### CONFLICT OF INTEREST STATEMENT

Authors declare no conflict of interests.

#### DATA AVAILABILITY STATEMENT

The data that supports the findings of this study are available in the supplementary material of this article.

#### ORCID

Javier Fernández-Lozano  <https://orcid.org/0000-0001-9741-3917>

Rosa M. Carrasco  <https://orcid.org/0000-0001-8762-6951>

#### REFERENCES

- Abermann, J., Fischer, A., Lambrecht, A., & Geist, T. (2010). On the potential of very high-resolution repeat DEMs in glacial and periglacial environments. *The Cryosphere*, 4(1), 53–65.
- Abolt, C. J., Young, M. H., & Caldwell, T. G. (2017). Numerical modelling of ice-wedge polygon geomorphic transition. *Permafrost and Periglacial Processes*, 28(1), 347–355.
- AEMET. (2023). Opendata. <https://opendata.aemet.es/centrodedescargas/inicio>
- Andrés-de Pablo, N., & Palacios-Estremera, D. (2010). Cobertura nival y distribución de la temperatura en el suelo en las cumbres de la Sierra de Guadarrama. *Cuadernos de Investigación Geográfica*, 36(2), 7–36.
- Arenas-Martínez, R., Fuster, J. M., Martínez-Salanova, J., del Olmo Sanz, A., & Villaseca, C. (1991). Mapa geológico de la Hoja nº 483 (Segovia). Mapa Geológico de España E 1:50.000.
- Ballantyne, C., & Harris, C. (1994). *The periglacial of Great Britain*. Cambridge University Press.
- Beerten, K., Meylemans, E., Kasse, C., Mestdagh, T., Van Rooij, D., & Bastiaens, J. (2021). Networks of unusually large fossil periglacial polygons, Campine area, northern Belgium. *Geomorphology*, 377, 107582.
- Bini, M., Zanchetta, G., Perşoiu, A., Cartier, R., Català, A., Cacho, I., Dean, J. R., Di Rita, F., Drysdale, R. N., Finnè, M., Isaola, I., Jalali, B., Lirer, F., Magri, D., Masi, D., Marks, L., Mercuri, A. M., Peyron, O., Sadori, L., ... Brisset, E. (2019). The 4.2 ka BP event in the mediterranean region: An overview. *Climate of the Past*, 15(2), 555–577.
- Bobachev, A. A., Shevnev, V. A., & Modin, I. N. (2003). IPI2WIN version 3.0.1e. <http://geophys.geol.msu.ru/ipi2win.htm>
- Carrasco, R. M., Pedraza, J., Fernández-Lozano, J., Sanchez-Vizcaíno, J., Soteres, R. L., Karampaglidis, T., Turú, V., Ros, X., & Merlo, O. (2020). El hidrolacolito de las Calderuelas (Parque Nacional de la Sierra de Guadarrama), una morfología periglacial singular. *Geogaceta*, 67, 91–94.
- Carrasco, R. M., Pedraza, J., & Palacios, D. (2022). The glaciers of the sierras de Guadarrama and Somosierra. In M. Oliva, D. Palacios, & J. M. Fernández-Fernández (Eds.), *Iberia, Land of glaciers* (pp. 485–503). Elsevier.
- Carrasco, R. M., Pedraza, J., Willenbring, J. K., Karampaglidis, T., Soteres, R. L., & Martín-Duque, J. F. (2016). Morfología glaciar del Macizo de Los Pelados-El Nevero (Parque Nacional de la Sierra de Guadarrama). Nueva interpretación y cronología. *Boletín de la Real Sociedad Española de Historia Natural*, 110, 1–16.
- Carrasco, R. M., Soteres, R. L., Pedraza, J., Fernández-Lozano, J., Turu, V., Antonio López-Sáez, J., Karampaglidis, T., Granja-Bruña, J. L., & Muñoz-Martín, A. (2020). Glacial geomorphology of the high Gredos massif: Gredos and Pinar valleys (Iberian central system, Spain). *Journal of Maps*, 16(2), 790–804.
- Carrasco, R. M., Turu, V., Pedraza, J., Munoz-Martin, A., Ros, X., Sanchez, J., Ruiz-Zapata, B., Olaiz, A., & Herrero-Simón, R. (2018). Near surface geophysical analysis of the Navamuño depression (sierra de Béjar, Iberian central system): Geometry, sedimentary infill and genetic implications of tectonic and glacial footprint. *Geomorphology*, 315, 1–16.
- Centeno, J. D., Pedraza, J., & Ortega, L. I. (1983). Estudio geomorfológico, clasificación del relieve de la Sierra de Guadarrama y nuevas aportaciones sobre su morfología glaciar. *Boletín de la Real Sociedad Española Historia Natural*, 81(3-4), 153–171.
- Colucci, R. R., Boccali, C., Žebre, M., & Guglielmin, M. (2016). Rock glaciers, protalus ramparts and pronaal ramparts in the south-eastern Alps. *Geomorphology*, 269, 112–121.
- Cummings, C. E., & Pollard, W. H. (1989). An investigation of palsas in the Schefferville area, Quebec. *Musk-Ox*, 37, 8–18.

- De la Barrera-Bautista, B., Boyd, D. S., Ledger, M., Siewert, M. B., Chandler, C., Bradley, A. V., Gee, D., Large, D. J., Olofsson, J., Sowter, A., & Sjögersten, S. (2022). Towards a monitoring approach for understanding permafrost degradation and linked subsidence in Arctic peatlands. *Remote Sensing*, 14(3), 444.
- De Vicente, G., Cunha, P. P., Muñoz-Martín, A., Cloetingh, S. A. P. L., Olaiz, A., & Vegas, R. (2018). The Spanish-Portuguese central system: An example of intense intraplate deformation and strain partitioning. *Tectonics*, 37(12), 4444–4469.
- De Vicente, G., Vegas, R., Martín, A. M., Silva, P. G., Andriessen, P., Cloetingh, S. A. P. L., González-Casado, J. M., Van Wees, J. D., Álvarez, J., Carbó, A., & Olaiz, A. (2007). Cenozoic thick-skinned deformation and topography evolution of the Spanish central system. *Global and Planetary Change*, 58(1–4), 335–381.
- Doneus, M. (2013). Openness as visualisation technique for interpretative mapping of airborne lidar derived digital terrain models. *Remote Sensing*, 5(12), 6427–6442.
- Doolittle, J., & Nelson, F. (2009). Characterising relict cryogenic macrostructures in mid-latitude areas of the USA with three-dimensional ground-penetrating radar. *Permafrost and Periglacial Processes*, 20(3), 257–268.
- Fernández-Lozano, J., & Andrés-Bercianos, R. (2020). On the origin of a remote mountainous natural reserve: Insights from a topo-bathymetry reconstruction of the glacial lake of Truchillas (NW Spain). *Quaternary International*, 566, 16–23.
- Fernández-Lozano, J., & Gutiérrez-Alonso, G. (2016). Improving archaeological prospection using localised UAVs assisted photogrammetry: An example from the Roman Gold District of the Eria River valley (NW Spain). *Journal of Archaeological Science: Reports*, 5, 509–520.
- Fernández-Lozano, J., Palao-Vicente, J. J., Blanco-Sánchez, J. A., Gutiérrez-Alonso, G., Remondo, J., Bonachea, J., Morellón, M., & González-Diez, A. (2019). Gold-bearing Plio-Quaternary deposits: Insights from airborne LiDAR technology into the landscape evolution during the early Roman mining works in north-West Spain. *Journal of Archaeological Science: Reports*, 24, 843–855.
- Fewster, R. E., Morris, P. J., Swindles, G. T., Gregoire, L. J., Ivanovic, R. F., Valdes, P. J., & Mullan, D. (2020). Drivers of Holocene palsa distribution in North America. *Quaternary Science Reviews*, 240, 106337.
- Franco-Múgica, F., García-Antón, M., & Sainz-Ollero, H. (1998). Vegetation dynamics and human impact in the sierra de Guadarrama, central system, Spain. *The Holocene*, 8(1), 60–82. <https://doi.org/10.1191/095968398675691171>
- French, H. M. (1996). *The periglacial environment* (2nd ed., p. 341). Addison Wesley Longman.
- Frenzel, B. (1959). Die Vegetations- und Landschaftszonen Nord-Eurasiens während der letzten Eiszeit und während der postglazialen Wärmezeit. I. Teil: Allgemeine Grundlagen. In: Steiner, F. (Ed.), *Abhandlungen der mathematisch-naturwissenschaftlichen Klasse. Mathematisch-Naturwissenschaftliche Klasse* (Vol. 13, pp. 937–1099). Verlag der Akademie der Wissenschaften und der Literatur.
- Gellatly, A. F., Grove, J. M., & Switsur, V. R. (1992). Mid-Holocene glacial activity in the Pyrenees. *The Holocene*, 2(3), 266–270.
- Granja-Bruña, J. L., Turu, V., Carrasco, R. M., Muñoz-Martín, A., Ros, X., Fernández-Lozano, J., Soteres, R. L., Karampaglidis, T., López-Sáez, J. A., & Pedraza, J. (2021). Geophysical characterization of the El Cervunal kame complex (sierra de Gredos, Iberian central system): Insight of infill geometry and reconstruction of former glacial formations. *Journal of Applied Geophysics*, 195, 104478.
- Groos, A. R., Niederhauser, J., Lemma, B., Fekadu, M., Zech, W., Hänsel, F., Wraase, L., Akár, N., & Veit, H. (2022). An hourly ground temperature dataset for 16 high-elevation sites (3493–4377 m a.s.l.) in the Bale Mountains, Ethiopia (2017–2020). *Earth System Science Data*, 14(3), 1043–1062.
- Harris, S. A., French, H. M., Heginbottom, J. A., Johnston, G. H., Ladanyi, B., Sego, D. C., & van Everdingen, R. O. (1988). *Glossary of permafrost and related ground-ice terms* (p. 156). National Research Council of Canada, Technical Memorandum No. 142.
- Haugerud, R. A., Harding, D. J., Johnson, S. Y., Harless, J. L., Weaver, C. S., & Sherrod, B. L. (2003). High-resolution lidar topography of the Puget lowland, Washington. *GSA Today*, 13(6), 4–10.
- Hausmann, J., Steinel, H., Kreck, M., Werban, U., Vienken, T., & Dietrich, P. (2013). Two-dimensional geomorphological characterization of a filled abandoned meander using geophysical methods and soil sampling. *Geomorphology*, 201, 335–343.
- Hendrickx, H., De Sloover, L., Stal, C., Delaloye, R., Nyssen, J., & Frankl, A. (2020). Talus slope geomorphology investigated at multiple time scales from high-resolution topographic surveys and historical aerial photographs (Sanetsch pass, Switzerland). *Earth Surface Processes and Landforms*, 45(14), 3653–3669.
- Hendrickx, H., Delaloye, R., Nyssen, J., & Frankl, A. (2017). Using UAV and SfM to understand the geomorphological dynamics on periglacial talus slopes. In *7th Belgian geography day*. Liège Université.
- Hernández-Molina, F. J., Somoza, L., Rey, J., & Pomar, L. (1994). Late Pleistocene-Holocene sediments on the Spanish continental shelves: Model for very high resolution sequence stratigraphy. *Marine Geology*, 120, 129–174.
- Holst, C., Janßen, J., Schmitz, B., Blome, M., Dercks, M., Schoch-Baumann, A., Blöthe, J., Schrott, L., Kuhlmann, H., & Medic, T. (2021). Increasing spatio-temporal resolution for monitoring alpine solifluction using terrestrial laser scanners and 3d vector fields. *Remote Sensing*, 13(6), 1192.
- Hopkinson, C., & Demuth, M. N. (2006). Using airborne lidar to assess the influence of glacier downwasting on water resources in the Canadian Rocky Mountains. *Canadian Journal of Remote Sensing*, 32(2), 212–222.
- Jalut, G., Michels, V. T., Dedoubat, J. J., Otto, T., Ezquerro, J., Fontugne, M., Belet, J. M., Bonnet, L., García de Celis, A., Redondo-Vega, J. M., Vidal-Romaní, J. R., & Santos, L. (2010). Palaeoenvironmental studies in NW Iberia (Cantabrian range): Vegetation history and synthetic approach of the last deglaciation phases in the western Mediterranean. *Palaeogeography, Palaeoclimatology, Palaeoecology*, 297(2), 330–350.
- Jones, B. M., Stoker, J. M., Gibbs, A. E., Grosse, G., Romanovsky, V. E., Douglas, T. A., Kinsman, N. E. M., & Richmond, B. M. (2013). Quantifying landscape change in an arctic coastal lowland using repeat airborne LiDAR. *Environmental Research Letters*, 8(4), 045025.
- Jónsson, S. A., Schomacker, A., Benediktsson, Í. Ö., Ingólfsson, Ó., & Johnson, M. D. (2014). The drumlin field and the geomorphology of the Múlajökull surge-type glacier, Central Iceland. *Geomorphology*, 207, 213–220.
- Kirpotin, S., Polishchuk, Y., Bryksina, N., Sugaipova, A., Kouraev, A., Zakharova, E., Pokrovsky, O. S., Shirokova, L., Kolmakova, M., Manassypov, R., & Dupre, B. (2011). West Siberian palsa peatlands: Distribution, typology, cyclic development, present day climate-driven changes, seasonal hydrology and impact on CO<sub>2</sub> cycle. *International Journal of Environmental Studies*, 68(5), 603–623.
- Kokalj, Z., Zakšek, K., & Oštir, K. (2011). Application of sky-view factor for the visualisation of historic landscape features in lidar-derived relief models. *Antiquity*, 85(327), 263–273.
- Kunz, J., & Kneisel, C. (2021). Three-dimensional investigation of an open and a closed-system pingo in northwestern Canada. *Permafrost and Periglacial Processes*, 32(4), 541–557.
- Leopold, M., & Völkel, J. (2003). GPR images of periglacial slope deposits beneath peat bogs in the central European highlands, Germany. *Geological Society, London, Special Publications*, 211(1), 181–189.
- Loke, M. H., Wilkinson, P. B., & Chambers, J. E. (2010). Parallel computation of optimised arrays for 2-D electrical imaging surveys. *Geophysical Journal International*, 183(3), 1302–1315.
- López-Sáez, J. A., Carrasco, R. M., Turu, V., Ruiz-Zapata, B., Gil-García, M. J., Luelmo-Lautenschlaeger, R., Pérez-Díaz, S., Alba-Sánchez, F., Abel-Schaad, D., Ros, X., & Pedraza, J. (2020). Late glacial-

- early holocene vegetation and environmental changes in the western Iberian central system inferred from a key site: The Navamuño record, Béjar range (Spain). *Quaternary Science Reviews*, 230, 106167.
- Luo, L., Ma, W., Zhang, Z., Zhuang, Y., Yang, J., Cao, X., Liang, S., & Yi, S. (2019). Integration of terrestrial laser scanning and soil sensors for deformation and hydrothermal monitoring of frost mounds. *Measurement*, 131, 513–523.
- Macaya, J., González-Lodeiro, F., Martínez-Catalán, J. R., & Álvarez, F. (1991). Continuous deformation, ductile thrusting and backfolding of cover and basement in the sierra de Guadarrama, Hercynian orogen of Central Spain. *Tectonophysics*, 191(3–4), 291–309.
- Mackay, J. (1979). Pingos of the Tuktoyaktuk peninsula area, northwest territories. *Géographie Physique et Quaternaire*, 33(1), 3–61.
- Mackay, J. (1998). Pingo growth and collapse, Tuktoyaktuk peninsula area, western Arctic coast, Canada: A long-term field study. *Géographie Physique et Quaternaire*, 52(3), 271–323.
- Mackay, J. R. (1972). The world of underground ice. *Annals of the Association of American Geographers*, 62(1), 1–22.
- Marcos, J., & Palacios, D. (2004). Efectos de la nieve y la temperatura del suelo en la actividad geomorfológico: Primeros resultados de su monitorización en la Sierra de Guadarrama (España). *Boletín de la Real Sociedad Española de Historia Natural (Sección Geología)*, 99(1–4), 25–36.
- Marcos, J., Úbeda, J., Andrés, N., & Palacios, D. (2022). A combination of cosmogenic and Schmidt hammer exposure dating in the study of the deglaciation timing of sierra de Guadarrama National Park (Spain). *Geografiska Annaler: Series A, Physical Geography*, 104(2), 70–89.
- Melón-Nava, A., Santos-González, J., Redondo-Vega, J. M., González-Gutiérrez, R. B., & Gómez-Villar, A. (2022). Factors influencing the ground thermal regime in a mid-latitude glacial cirque (Hoyo Empeadrado, Cantabrian Mountains, 2006–2020). *Catena*, 212, 106110.
- Migoñ, P., Kasprzak, M., & Traczyk, A. (2013). How high-resolution DEM based on airborne LiDAR helped to reinterpret landforms: Examples from the Sudetes, SW Poland. *Landform Analysis*, 22, 89–101.
- Molina, E., & Pellitero, E. (1982). Formas periglaciares actuales en la Paramera de Avila, Hipótesis sobre su génesis. *Boletín de la Real Sociedad Española de Historia Natural, Sección Geológica Madrid*, 80, 49–56.
- Morales-Molino, C., García-Antón, M., Postigo-Mijarra, J. M., & Morla, C. (2013). Holocene vegetation, fire and climate interactions on the westernmost fringe of the Mediterranean Basin. *Quaternary Science Reviews*, 59, 5–17.
- Munroe, J. S., Doolittle, J. A., Kanevskiy, M. Z., Hinkel, K. M., Nelson, F. E., Jones, B. M., Shur, Y., & Kimble, J. M. (2007). Application of ground-penetrating radar imagery for three-dimensional visualisation of near-surface structures in ice-rich permafrost, Barrow, Alaska. *Permafrost and Periglacial Processes*, 18(4), 309–321.
- Murton, J. B. (2021). What and where are periglacial landscapes? *Permafrost and Periglacial Processes*, 32(2), 186–212.
- Oliva, M., Antoniades, D., Serrano, E., Giralt, S., Liu, E. J., Granados, I., Plarabes, S., Toro, M., Gyu-Hong, S., & Vieira, G. (2019). The deglaciation of Barton peninsula (king George Island, south Shetland islands, Antarctica) based on geomorphological evidence and lacustrine records. *Polar Record*, 55(3), 177–188.
- Oliva, M., Serrano, E., Gómez-Ortiz, A., González-Amuchastegui, M. J., Nieuwendam, A., Palacios, D., Pérez-Alberti, A., Pellitero-Ondicol, R., Ruiz-Fernández, J., Valcárcel, M., Vieira, G., & Antoniades, D. (2016). Spatial and temporal variability of periglaciation of the Iberian Peninsula. *Earth-Science Reviews*, 137, 176–199.
- Oliva, M., Žebre, M., Guglielmin, M., Hughes, P. D., Çiner, A., Vieira, A., Bodin, X., Andrés, N., Colucci, R. R., García-Hernández, C., Mora, C., Nofre, J., Palacios, D., Pérez-Alberti, A., Ribolini, A., Ruiz-Fernández, J., Sarikaya, M. A., Serrano, E., Urdea, P., ... Yildirim, C. (2018). Permafrost conditions in the Mediterranean region since the last glaciation. *Earth-Science Reviews*, 185, 397–436.
- Olvmo, M., Holmer, B., Thorsson, S., Reese, H., & Lindberg, F. (2020). Subarctic palsa degradation and the role of climatic drivers in the largest coherent palsa mire complex in Sweden (Vissátvuopmi), 1955–2016. *Scientific Reports*, 10(1), 1–10.
- Palacios, D., de Andrés, N., de Marcos, J., & Vázquez-Selem, L. (2012). Glacial landforms and their paleoclimatic significance in sierra de Guadarrama, Central Iberian Peninsula. *Geomorphology*, 139, 67–78.
- Palacios, D., de Andrés, N., & Luengo, E. (2003). Distribution and effectiveness of nivation in Mediterranean mountains: Peñalara (Spain). *Geomorphology*, 54, 157–178.
- Palomo-Segovia, M. (2012). *Temperatura del suelo en las cumbres de la Sierra de Guadarrama*. (p. 113) [Tesis Doctoral, Universidad Complutense de Madrid, Madrid].
- Pedraza, J. (1987). Geología y relieve. In: La naturaleza de Madrid. Fernández-Galiano, E. & Ramos-Fernández, A. (Eds.). *Consejería de Agricultura y Ganadería*. Comunidad de Madrid, Madrid. 11–67.
- Pedraza, J. (1994). Periglacialismo del sistema central español. In M. Simón-Torres, A. Gómez-Ortiz, & F. Salvador-Frach (Eds.), *Periglacialismo en la Península Ibérica, Canarias y Baleares: Estudios significativos* (pp. 147–164). Universidad de Granada.
- Pissart, A. (1994). *Fossil pingos of Wales and the Hautes Fagnes, Belgium*. John Wiley & Sons.
- Pollard, W. H., & French, H. M. (1984). The groundwater hydraulics of seasonal frost mounds, north fork pass, Yukon territory. *Canadian Journal of Earth Sciences*, 21(10), 1073–1081.
- Prima, O. D. A., & Yoshida, T. (2010). Characterization of volcanic geomorphology and geology by slope and topographic openness. *Geomorphology*, 118(1–2), 22–32.
- Reimer, P. J., Austin, W. E., Bard, E., Bayliss, A., Blackwell, P. G., Ramsey, C. B., Butzin, M., Cheng, H., Edwards, L., Friedrich, M., Grootes, P., Guilderson, T., Hajdas, I., Heaton, T., Hogg, A., Hughen, K., Kromer, B., Manning, S., Muscheler, R., ... Talamo, S. (2020). The IntCal20 northern hemisphere radiocarbon age calibration curve (0–55 cal kBP). *Radiocarbon*, 62(4), 725–757.
- Reynolds, J. M. (2011). *An introduction to applied and environmental geophysics* (p. 710). John Wiley & Sons.
- Robson, B. A., MacDonell, S., Ayala, Á., Bolch, T., Nielsen, P. R., & Vivero, S. (2022). Glacier and rock glacier changes since the 1950s in the La Laguna catchment, Chile. *The Cryosphere*, 16(2), 647–665.
- Ross, N. (2013). Frost mounds: Active and relict forms. In S. A. Elias & C. J. Mock (Eds.), *The Encyclopedia of Quaternary Science* (pp. 472–480). Elsevier.
- Ruiz-García, C., Rodríguez-Fernández, L. R., & Pérez-González, A. (Eds.). (1991). *Mapa Geológico de España 1:50.000, hoja nº 483 (Segovia) y memoria* (p. 135). IGME.
- Salazar-Rincón, A., Mata-Campo, P., Rico-Herrera, M. T., Valero-Garcés, B. L., Oliva-Urcía, B., Ibarra, P., Rubio, F. M., & Grupo Horda. (2013). El paleolago de La Larri (valle de Pineta, Pirineos): Significado en el contexto del último máximo glaciar en el Pirineo. *Cuadernos de Investigación Geográfica. Universidad de La Rioja*, 39(1), 81–100.
- Schennen, S., Tronicke, J., Wetterich, S., Allroggen, N., Schwamborn, G., & Schirrmeyer, L. (2016). 3D ground-penetrating radar imaging of ice complex deposits in northern East Siberia. *Geophysics*, 81(1), WA195–WA202.
- Schrott, L., & Sass, O. (2008). Application of field geophysics in geomorphology: Advances and limitations exemplified by case studies. *Geomorphology*, 93(1–2), 55–73.
- Seppälä, M. (1986). The origin of palsas. *Geografiska Annaler: Series A, Physical Geography*, 68(3), 141–147.
- Serrano, E., de Sanjosé-Blasco, J. J., Gómez-Lende, M., López-Moreno, J. I., Pisabarro, A., & Martínez-Fernández, A. (2019). Periglacial environments and frozen ground in the central Pyrenean high mountain area: Ground thermal regime and distribution of landforms and processes. *Permafrost and Periglacial Processes*, 30(4), 292–309.
- Serrano, E., López-Moreno, J. I., Gómez-Lende, M., Pisabarro, A., Martín-Moreno, R., Rico, I., & Alonso-González, E. (2020). Frozen ground and periglacial processes relationship in temperate high mountains: A case

- study at Monte Perdido-Tucarroya area (the Pyrenees, Spain). *Journal of Mountain Science*, 17(5), 1013–1031.
- Serrano, E., Oliva, M., González-García, M., López-Moreno, J. I., González-Trueba, J., Martín-Moreno, R., Gómez-Lende, M., Martín-Díaz, J., Nofre, J., & Palma, P. (2018). Post-little ice age paraglacial processes and landforms in the high Iberian mountains: A review. *Land Degradation & Development*, 29(11), 4186–4208.
- Śledź, S., Ewertowski, M. W., & Piekarczyk, J. (2021). Applications of unmanned aerial vehicle (UAV) surveys and structure from motion photogrammetry in glacial and periglacial geomorphology. *Geomorphology*, 378, 107620.
- Štular, B., Kokalj, Ž., Oštir, K., & Nuninger, L. (2012). Visualization of lidar-derived relief models for detection of archaeological features. *Journal of Archaeological Science*, 39(11), 3354–3360.
- Turu, V. (2023). *Mid-late Pleistocene glacial dynamics in the Valira valleys (Principality of Andorra). Asymmetries within the Pyrenees and correlation across the westernmost European mountain ranges.* (p. 500) [PhD Thesis, University of Barcelona].
- Turu, V., Carrasco, R. M., López-Sáez, J. A., Pontevedra-Pombal, X., Pedraza, J., Luelmo-Lautenschlaeger, R., Pérez-Díaz, S., Echeverría-Moreno, A., Frigola, J., Alba-Sánchez, F., Sánchez-Vizcaino, J., Pélachs-Mañosa, A., Cunill-Artigas, R., Nadal-Tersa, J., Mur-Cacaho, E., & Soriano-López, J. M. (2021). Palaeoenvironmental changes in the Iberian central system during the late-glacial and Holocene as inferred from geochemical data: A case study of the Navamuño depression in western Spain. *Catena*, 207, 105689.
- Turu, V., Carrasco, R. M., Pedraza, J., Ros, X., Ruiz-Zapata, B., Soriano-López, J. M., Mur-Cacaho, E., Pélachs-Mañosa, A., Muñoz-Martín, A., Sánchez, J., & Echeverría-Moreno, A. (2018). Late glacial and post-glacial deposits of the Navamuño peatbog (Iberian central system): Chronology and paleoenvironmental implications. *Quaternary International*, 470, 82–95.
- Turu, V., Peña-Monné, J. L., Cunha, P. P., Jalut, G., Buylaert, J. P., Murray, A. S., Bridgland, D., Faurischou-Knudsen, M., Oliva, M., Carrasco, R. M., Ros, X., Turu-Font, L., & Ventura-Roca, J. V. (2023). Glacial-interglacial cycles in the south-central and southeastern Pyrenees since ~180 ka (NE Spain–Andorra–S France). *Quaternary Research*, 113, 1–28.
- Van Everdingen, R. O. (Ed.). (1998). Multi-language glossary of permafrost and related ground-ice terms. In *IPA and the Arctic Institute of North America* (p. 159). The University of Calgary (revised 2005).
- Vieira, G. T., Mora, C., & Ramos, M. (2003). Ground temperature regimes and geomorphological implications in a Mediterranean mountain (Serra da Estrela, Portugal). *Geomorphology*, 52(1–2), 57–72.
- Voelkel, J., Leopold, M., & Roberts, M. C. (2001). The radar signatures and age of periglacial slope deposits, central highlands of Germany. *Permafrost and Periglacial Processes*, 12(4), 379–387.
- Walker, M. (2005). *Quaternary dating methods* (p. 279). John Wiley and Sons.
- Ward, S. (2004). Hydro-laccolith. In A. S. Godie (Ed.), *Encyclopaedia of geomorphology*, V1 (p. 539). Routledge.
- Washburn, A. L. (1979). *Geocryology* (p. 397). Edward Arnold.
- Woolderink, H. A. G. (2014). *Late Weichselian permafrost distribution and degradation. A pingo based reconstruction for The Netherlands.* (p. 84) [PhD Dissertation Thesis, Utrecht University].
- Worsley, P. (2004). Periglacial geomorphology. In A. S. Godie (Ed.), *Encyclopedia of geomorphology*, Vol. 1 (pp. 772–776). Routledge.
- Wright, H. E., Mann, D. H., & Glaser, P. H. (1984). Piston corers for peat and lake sediments. *Ecology*, 65(2), 657–659.
- Zakšek, K., Oštir, K., & Kokalj, Ž. (2011). Sky-view factor as a relief visualization technique. *Remote Sensing*, 3(2), 398–415.

## SUPPORTING INFORMATION

Additional supporting information can be found online in the Supporting Information section at the end of this article.

**How to cite this article:** Fernández-Lozano, J., Turu, V., Carrasco, R. M., Soteres, R. L., Sánchez-Vizcaino, J., Karampaglidis, T., Ros, X., Merlo, O., & Pedraza, J. (2024). The mid-latitude hydrolaccolith of the Spanish Central System (Southern Europe): A top-to-bottom integration of geomatic, geophysical and sedimentary datasets for characterising a singular periglacial landform. *Land Degradation & Development*, 35(3), 1029–1049. <https://doi.org/10.1002/ldr.4968>